

Article

A Relief Dependent Evaluation of Digital Elevation Models on Different Scales for Northern Chile

Tanja Kramm and Dirk Hoffmeister * 

GIS and Remote Sensing, Institute of Geography, University of Cologne, Albertus Magnus Platz, 50923 Köln, Germany; tanja.kramm@uni-koeln.de

* Correspondence: dirk.hoffmeister@uni-koeln.de

Received: 29 August 2019; Accepted: 27 September 2019; Published: 28 September 2019



Abstract: Many geoscientific computations are directly influenced by the resolution and accuracy of digital elevation models (DEMs). Therefore, knowledge about the accuracy of DEMs is essential to avoid misleading results. In this study, a comprehensive evaluation of the vertical accuracy of globally available DEMs from Advanced Spaceborne Thermal Emission and Reflection Radiometer (ASTER), Shuttle Radar Topography Mission (SRTM), Advanced Land Observing Satellite (ALOS) World 3D and TanDEM-X WorldDEM™ was conducted for a large region in Northern Chile. Additionally, several very high-resolution DEM datasets were derived from Satellite Pour l'Observation de la Terre (SPOT) 6/7 and Pléiades stereo satellite imagery for smaller areas. All datasets were evaluated with three reference datasets, namely elevation points from both Ice, Cloud, and land Elevation (ICESat) satellites, as well as very accurate high-resolution elevation data derived by unmanned aerial vehicle (UAV)-based photogrammetry and terrestrial laser scanning (TLS). The accuracy was also evaluated with regard to the existing relief by relating the accuracy results to slope, terrain ruggedness index (TRI) and topographic position index (TPI). For all datasets with global availability, the highest overall accuracies are reached by TanDEM-X WorldDEM™ and the lowest by ASTER Global DEM (GDEM). On the local scale, Pléiades DEMs showed a slightly higher accuracy as SPOT imagery. Generally, accuracy highly depends on topography and the error is rising up to four times for high resolution DEMs and up to eight times for low-resolution DEMs in steeply sloped terrain compared to flat landscapes.

Keywords: accuracy assessment; digital terrain model; stereo satellite imagery; topography; terrestrial laser scanning; topographic position index; terrain ruggedness index; unmanned aerial vehicles

1. Introduction

Relief plays a main role for numerous geomorphological, climatic, hydrologic and ecologic processes. Therefore, a detailed understanding of the prevailing terrain conditions is essential [1]. Nowadays, geomorphometric relief information is available by digital elevation models (DEMs), which provide a 2.5 dimensional digital representation of the Earth's relief using regularly spaced elevation data.

The first digital elevation datasets with a global coverage were DEMs from the Shuttle Radar Topography Mission (SRTM) and the Advanced Spaceborne Thermal Emission and Reflection Radiometer (ASTER) with a resolution of 30 m, which have revolutionized the use of DEMs [2,3]. While analyses in former times only were possible for small areas, these DEMs enabled the possibility of analyzing larger surface areas up to almost the whole Earth. In recent years, the Advanced Land Observing Satellite (ALOS) World 3D as a third global DEM with a ground sampling distance (GSD) of 30 m was made publicly available [4,5]. The most recent dataset with global coverage is the TanDEM-X World DEM™ dataset with a GSD of 12 m, which is expected to be the new standard in geometric

resolution and accuracy [6,7]. However, all of these DEMs usually are less accurate and capture less terrain details due to lower GSD in comparison to very high-resolution elevation models derived by stereo satellite imagery. These datasets normally have a higher GSD and vertical accuracy. However, they are often not suitable for larger areas, due to high cost and time-consuming processing. Therefore, these are only usable for large scale analyses.

Elevation models generally enable the possibility of a quantitative characterization of relief and are used by geomorphometry as a multifaceted interdisciplinary subject in a multitude of different scientific fields [8]. Hence, DEMs are widely used sources in numerous geospatial studies for the terrain-based identification of environmental features. Many studies about landform distribution analyses [9–13], geomorphology [14] and the human impact on geomorphology [15] were conducted. Furthermore, in the field of hydrology DEMs are required for stream network analysis [16,17] and ground-water flow modelling [18]. Terrain features derived by DEMs are also used as a predictor for digital soil mapping [19–21]. Additionally, DEMs are crucial for ecological analysis, such as vegetation and plant distribution research [22–24]. Climatic issues, like the observation of glacier changes [25], sea-level rise [26] or climatic modelling [27] are also fields of application, where terrain information is needed.

All of these applications have raised increasing needs for accessible DEMs of higher resolution and accuracy. However, if the process or object of interest is spatially smaller than the GSD of the utilized elevation datasets, the risk of misleading results increases [28]. Likewise, it is well known, that the GSD of a digital elevation model directly influences derived terrain variables such as slope or aspect. For instance, Kienzle [29] showed that the mean slope can differ from 13.9% on a 50 m grid to 8.8% on a 250 m resolution DEM. This effect even increases for higher resolutions and steeper terrain. Zhang and Montgomery [30] derived mean slope differences of up to 24% between a 2 m and a 90 m DEM for the same area. Kramm et al. [11] showed that the accuracy of detected landforms might range up to 30% for the same algorithm and area by using DEMs in different resolutions. Likewise, also different DEMs with the same grid size result in significant differences in the delineated landforms.

Thus, the effects of scale and the impact of the DEMs GSD when deriving topographical features are well documented [31–34] and also the first techniques for multiscale analysis are available [35–37]. Furthermore, it is crucial to analyze the accuracy of DEMs to select the most suitable regarding aim, accuracy and scale of the study. Large-channel profiles over wide distances are easily possible to identify even with 90 m resolution data, landscapes in large scales require elevation data with 1–30 m GSD for a successful identification of individual hillslopes and ridges [38,39]. However, a DEM with a higher GSD is not always advantageous, as elevation models with a very high resolution can depict too many details, which are not relevant for the study.

In recent years, numerous studies have investigated the accuracy of available DEMs. Much research was already done on the accuracy of SRTM and ASTER Global DEM to examine their performance in different situations and sites [40–44]. All of these investigations indicate that the expectable root mean square error (RMSE) for the ASTER GDEM is about 3–4 m in flat terrain and 7–8 m with up to 16 m (RMSE) in steeper relief. For the SRTM1 DEM the results show an average error of 3–4 m in flat landscapes up to 7–8 m in mountainous areas. Additionally, the accuracy of the newer ALOS World 3D [45] and the TanDEM-X World DEM™ [46–48] was assessed by comparing them with various reference datasets. Several studies directly compared the performance of different global elevation models in various geographical settings. The accuracy of the 30 m resolution DEMs from SRTM, ASTER Global DEM and ALOS W3D was assessed by many studies [49–54]. They indicate a slightly higher accuracy of ALOS W3D in comparison to SRTM and ASTER GDEM. The result showed an average error of 2–3 m (RMSE) in flat terrain and 6–7 m (RMSE) in steeper sloped landscapes for the ALOS W3D. However, less studies are available yet which compare the performance of the newly available TanDEM-X World DEM™ with other globally available DEMs. Some studies investigated the accuracy of TanDEM-X World DEM™ with elevation models from SRTM and ASTER Global DEM [55–57]. Others compared the accuracy of SRTM, ASTER GDEM, ALOS World 3D and TanDEM-X World DEM

™ for coastal relief settings [26,58] or for relative small areas [59,60]. They all showed a relative high performance of the TanDEM-X World DEM™ which is mostly superior to the accuracy of the 30 m global DEMs. The results indicate an average error of less than 3 m for the 12 m TanDEM-X World DEM™, but some recent studies also showed weaknesses of this DEM in very steep terrain [57].

Nevertheless, a comprehensive analysis of the accuracy of all four global DEMs over large areas is still missing. Furthermore, fewer studies evaluated the accuracy of DEMs on different scales and compared them to very high resolution elevation models derived by stereo satellite imagery. Alganci et al. [50] included some local DEMs derived by Satellite Pour l'Observation de la Terre (SPOT) and Pléiades satellite imagery in their study for an urban area with anthropogenic landscape. Thus, an analysis of the performance of these DEMs in a landscape which is not anthropogenic influenced is still missing.

The goal of this study is to conduct a comprehensive accuracy assessment of the vertical accuracy for a multitude of different DEMs, both for a regional coverage and for local coverages. The regional coverage for the selected study area, the Atacama Desert in northern Chile, is given by datasets with a nearly global coverage, namely the TanDEM-X World DEM™, ASTER Global DEM, ALOS World 3D and SRTM DEM. Local areas are covered by DEMs derived from stereo-satellite imagery recorded by SPOT 6/7 and Pléiades satellites with areas of 100 to 400 km². The accuracy assessment was performed with three control datasets, which are the light detection and ranging (LiDAR)-based elevation points from both Ice, Cloud, and land Elevation (ICESat) satellites and very accurate high-resolution elevation data derived by unmanned aerial vehicle (UAV)-based photogrammetry, as well as terrestrial laser scanning (TLS). The accuracy analysis is based on the root mean squared error (RMSE) and normalized median absolute deviation (NMAD). Furthermore, fewer studies have systematically investigated the influence of different terrain conditions on the vertical accuracy of DEMs. Some work has been done to investigate the appropriateness of DEMs for delineating different landforms [55] and the relationship of DEM errors in correlation to various landform types and altitude [61]. Additionally, the accuracy of DEMs for several small areas with plain, hilly and mountainous terrain [49] and with different slopes [57] was assessed. Nevertheless, more information about the impact of relief over larger areas on the vertical accuracy of DEMs is necessary. Thus, in this study the accuracy is addressed and evaluated with regard to the existing topography by linking terrain ruggedness index (TRI), topographic position index (TPI) and slope to error values, as terrain has a direct influence in accuracy [42,62,63].

2. Study Area

The study was conducted in the northern part of Chile (Figure 1). The area covers the Chilean part of the Atacama Desert, represented by the administrative regions of Tarapacá and Antofagasta. The region, which is one of the driest areas on Earth, is characterized by its hyperarid climate with less than 10 mm/year rainfall on average [64] lying in the 'Arid Diagonal' of South America. This hyperaridity of the Atacama is caused by a combination of subtropical subsidence, coastal upwelling of the cold Humboldt current, and rain-shadow effects of the high Andes [65], which might have been established since the mid-Miocene or earlier [66].

The relief shows large height differences from the coast of the Pacific to the mountains of the Andes with altitudes up to 6700 m above sea level. Furthermore, the study area consists of a diverse topography with steep, seaward cliffs and deeply incised canyons, as well as large alluvial fans and volcanos in the mountain range of the Andes. Thus, the landscape offers a cross section of different relief types from flat and broad landscapes to steep and dissected terrain, with hardly any vegetation cover. The morphodynamic zonation of the Atacama from west to east is described by the coastal ranges with the coastal cordillera reaching up to 2500 m above sea level, the central depression at about 1000 m above sea level and the pre-Andean or western cordillera, as well as the Altiplano (~3800 m above sea level). DEMs are for instance used for geomorphometric analysis of alluvial fans at the coastal range [67], as well as the geomorphometric characterization of the unique, so-called zebra stone stripes, described as contour-parallel bands of dark gravels with contrasting bands of fine-grained soil [68].

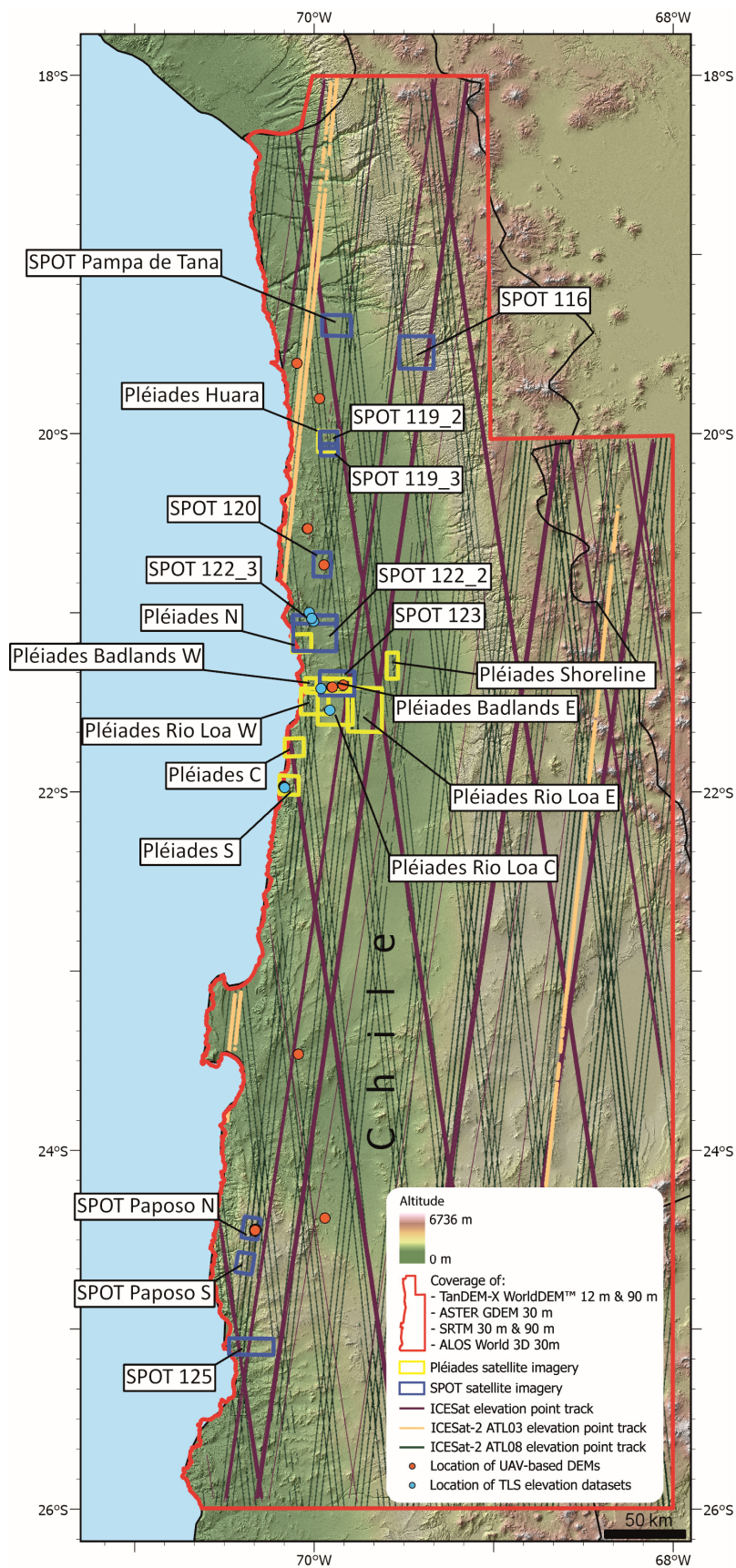


Figure 1. Overview map of study area and locations of digital elevation models (DEMs) and ground truth data. Map based on Shuttle Radar Topography Mission (SRTM) elevation data.

3. Materials and Methods

3.1. Global Digital Elevation Models (GDEMs)

The accuracy of several DEMs with a global coverage was validated in this study that are described in the following sections. Except for the 12 m TanDEM-X WorldDEM™, all utilized DEMs are freely available. All of these DEMs were evaluated for an area of around 190,000 km² (Figure 1). To make the heights of all DEMs comparable, a conversion to the same vertical datum is essential. Therefore, in this study all elevation models were converted to the WGS84 ellipsoid as vertical datum.

3.1.1. Advanced Spaceborne Thermal Emission and Reflection Radiometer (ASTER) GDEM

The ASTER Global DEM was produced by processing the entire optical imagery archive from the ASTER sensor onboard of National Aeronautics and Space Administration's (NASA) Earth Observing System Terra satellite, which was launched in December 1999 [3,69]. The mission's aim was primarily to collect multispectral data of the Earth, but in addition to the multispectral bands, the ASTER sensor has a near infrared sensor, which is inclined by 27.6° and enables stereoscopic recording according to the "as-track" principle [70].

A first version of this dataset was released for open access in June 2009 by the NASA and the Japanese Ministry of International Trade and Industry covering all land areas from 83° N to 83° S latitude. The second Version was released in October 2011 with a GSD of 1 arc-second (~30 m). It includes additional scenes from 2008 to 2011 and an improved water mask to achieve various improvements in overall accuracy and to reduce artifacts mainly caused by cloud edges [3]. The last update was created by including even more Level 1-A ASTER scenes acquired between March 2000 and November 2013 and conducting a more effective cloud masking to reduce artifacts. Furthermore, voids were filled with additional data from SRTM1 and the Global Multi-resolution Terrain Elevation Data 2010 (GMTED2010) for most areas of the world. The average vertical accuracy of the ASTER GDEM Version 3 was estimated with a standard deviation of 12.1 m, which is 0.5 m superior than for the prior version [71].

The utilized ASTER GDEM Version 3 in this contribution was originally referenced horizontally to the World Geodetic System 1984 (WGS84) and vertically to the Earth Gravitational Model 1996 (EGM96). Thus, the DEM was converted to WGS84 ellipsoid with a calculated raster of the undulation between EGM96 geoid and WGS84 ellipsoid for the whole region. The creation of the undulation raster was done with the software MSP GEOTRANS v.3.8. To do so, a net of points, which were equally distributed over the whole area was created for which the undulation was calculated by the software. Subsequently, a raster was processed by interpolating the undulation points with Kriging algorithm. Finally, the heights of the undulation raster were added to the ASTER GDEM heights.

3.1.2. Advanced Land Observing Satellite (ALOS) World 3D

The ALOS was launched in 2006 by the Japan Aerospace Exploration Agency (JAXA). Onboard of the satellite was the Panchromatic Remote-sensing Instrument for Stereo Mapping (PRISM) sensor which operated from 2006 to 2011 with the aim to generate global elevation data from along-track triplet stereoscopic panchromatic images with 2.5 m GSD [4,72]. During the sensor's operation time, approximately 6.5 million scenes, covering the entire globe, were produced which were used to generate a global DEM with a GSD of 5 m. To check data quality during the generation process an automatic check by comparing the data with reference information of ICESat GLAH14 heights and SRTM as well as by visual human interpretations was conducted to achieve a target height accuracy of 5 m [4]. Besides the 5 m DEM, which is only distributed commercially, JAXA released a freely available 1 arc-second (~30 m) ALOS DEM for non-commercial purposes in 2016, which was produced by resampling the original 5 m version [73]. The provided ALOS World 3D (W3D) dataset (Version 1), which was used in this study, is already referenced to WGS84 horizontal and WGS84 ellipsoidal vertical datum. Therefore, no further georeferencing was necessary for this dataset.

3.1.3. Shuttle Radar Topography Mission (SRTM)

While the previously presented ASTER and ALOS DEMs were generated by passive remote sensing techniques, the SRTM recorded actively the Earth's surface in February 2000 with two synthetic aperture radar systems. A C-band system (5.6 cm, SIR-C), operated by NASA's Jet Propulsion Laboratory (JPL) and a X-band system (3.1 cm, X-SAR), controlled by the German Aerospace Centre (DLR), and the Agenzia Spaziale Italiana (ASI, Italy) scanned the Earth for 11 days with the aim to map its topography between latitudes 60° N and 60° S [2].

A first global DEM version of the C-band data was released by the USGS in 2003 with a GSD of 3 arc-second. Furthermore, a DEM with 1 arc-second resolution was made available, but at first only for the US. For the rest of the world SRTM DEM data with 1 arc-second resolution followed in 2015. Since their initial release the SRTM-1 and SRTM-3 datasets have been continuously improved in several versions. In 2003 the data was initially published unprocessed, i.e. they contained regions without data or with incorrect elevation information. Furthermore, any processing of coastlines and water bodies was missing, which took place in a revised second version. In a third revised version, regions without data were filled mainly with elevation data from ASTER GDEM2 [74]. For the SRTM-3 dataset a 4th version was processed by the Consultative Group of International Agricultural Research-Consortium for Spatial Information (CGIAR-CSI), which used various interpolation techniques described by Reuter et al. [75] and extra auxiliary DEM data for void filling (CGIAR CSI).

The overall accuracy of the SRTM DEM is determined by Farr et al. [2] with an absolute vertical height error of 6.2 m and a relative height error of 5.5 m for South America. The horizontal positional accuracy was assessed with an absolute geolocation error of 9.0 m. In this contribution, the SRTM-1 Version 3 DEM with a GSD of 30 m and a SRTM-3 Version 4.1 dataset with 90 m resolution were used. Both are referenced horizontally to WGS84 and vertically to the EGM96 geoid. The conversion to a vertical WGS84 datum was done analogous as described for the ASTER GDEM dataset.

3.1.4. TanDEM-X World DEM™

The TanDEM-X mission from 2010 to 2015 was launched as a public-private effort between the DLR and Airbus Defence and Space to produce a precise global DEM between the latitudes 90° N and 90° S with higher accuracy and resolution than the recently existing ones. The Earth was measured from two satellites (TerraSAR-X and TanDEM-X) in a controlled orbit with a baseline of 250–500 m with X-band radar interferometry (InSAR) [7,76]. The TanDEM-X WorldDEM™, which is subsequently denoted as 'TanDEM-X', was produced in the original Version with 0.4 arc-seconds (~12 m) GSD as a commercial product of the TanDEM-X mission. The DEM heights were calibrated with heights of the ICESat GLA14 data product [46]. Furthermore, a 1 arc-second (~30 m) version was generated from the unweighted mean values of the underlying 12 m pixels (Wessel, 2016). Additionally, a 3 arc-seconds (~90 m) elevation model has been released by the DLR in 2018, which is free of charge for use in academic research. This DEM was also created by resampling the original 0.4 arc-second dataset.

The originally intended accuracy for the produced TanDEM-X DEM was an absolute error of less than 10 m in horizontal and vertical direction [46,60,77]. Several studies showed that the DEM product reaches this goal [7,46]. However, they indicate that the accuracy is even higher than originally assumed. For the 90 m DEM only few studies are available yet, which investigated its accuracy, but they suppose a higher accuracy than the SRTM 90 m DEM [47,78].

In this study the TanDEM-X DEM was used in two different resolutions of 12 m and 90 m. The horizontal datum for both DEMs is WGS84 and the heights were already referenced to WGS84 ellipsoid heights.

3.2. Local Digital Elevation Models

In addition to the globally available elevation models with lower spatial resolution, 10 elevation models were derived from Pléiades satellite stereo imagery, seven DEMs from SPOT 6 and four

from SPOT 7 satellite imagery. The DEMs are distributed over the whole area, depicted in Figure 1, and each DEM covers an area of about 100–400 km². These datasets were processed with the software PCI Geomatica 2018 OrthoEngine with automatic ground control point (GCP) and Tie-Point collection. For the GCP collection process, an additional orthorectified image was used to improve the accuracy of extracted GCPs. The orthorectified image was calculated with provided rational polynomial coefficients (RPCs) information and elevation data from the TanDEM-X 12 m DEM to reduce topographical distortions in the original satellite images. For each dataset around 80 GCPs and 50 tie-points were extracted. The points were checked manually to receive a calculated residual error of less than 1 m (RMSE). All derived elevation models were resampled to 5 m during the generation process to avoid small artifacts in the DEM product.

3.2.1. Pléiades

The Pléiades system consists of a constellation of two satellites operated by the French Space Center (CNES) and ASTRIUM GEO-Information Services. The first satellite (Pléiades 1A) was brought into a sun-synchronous orbit on 16 December 2011. The second one (Pléiades 1B) followed on 2 December 2012 [79]. Both satellites are equipped with optoelectronic, charge-coupled device (CCD) scanners, which scan the Earth's surface transversely to the direction of flight and convert the measured radiation into a measurable electrical signal. It is recorded in a panchromatic channel and four multispectral channels each with five line sensors [80,81]. The line sensors of the panchromatic sensor have a width of more than 6000 pixels and the multispectral sensors have a resolution of 1500 pixels. Thus, the satellite achieves a GSD of 0.5 m in the panchromatic channel and 2 m in the multispectral channels [79]. The Pléiades satellites thus belong to the satellite systems with a very high GSD. The positional accuracy is indicated with 8.5 m at nadir and 10.5 m within an angle of 30°. Due to the high agility of the satellites, the Pléiades system is able to acquire three or more nearly synchronous images of the same area [82,83].

3.2.2. Satellite Pour l'Observation de la Terre (SPOT) 6/7

The SPOT 6 satellite was launched in 2012 by EADS Astrium, SPOT 7 followed in 2014. Both satellites operate with high-resolution pushbroom sensors and record images in one panchromatic channel and four multispectral channels. They are able to produce images with a GSD of 1.5 m in the panchromatic and of 6 m in the multispectral channels [84]. They also have the capability of tri stereo imaging. The expectable geolocation accuracy for SPOT image products with Primary standard, which are also used in this study is stated with a circular error less than 10 m at the 90th percentile [84].

3.3. Ground Truth Elevation Data

For a vertical accuracy assessment, highly accurate evaluation data is necessary that should be at least three times more accurate than the evaluated dataset [85]. In this study the evaluation check was conducted by comparing the DEM heights with several highly accurate elevation data, which are described in the following.

3.3.1. Ice, Cloud, and Land Elevation satellite (ICESat)

The primary goal of NASA's ICESat mission was to observe the cryosphere and to measure changes in the polar ice sheet mass balance [86]. One of the utilized instruments of the ICESat satellite is the Geoscience Laser Altimeter System (GLAS) which has a 1064 nm laser channel for surface altimetry measurements [87]. It operated between February 2003 and October 2009 and the surface elevation data was measured during two to three observation periods each year of about 1 month each. The laser footprints have 172 m spacing along-track, and approximately 42 km cross-track spacing [86,87].

During its operation period ICESat has acquired a huge database of raw and processed data organized in 15 data products. Of interest for this contribution is the 14th product ICESat/GLA14 data, as this dataset contains highly accurate elevation data with a vertical accuracy of 0.1 m for flat locations

and 1 m for undulated terrain [86,88]. Thus, several studies showed a successful vertical accuracy assessment over a broader regional extent with ICESat data [89,90].

The ICESat/GLA14 land surface elevation data points originally provided were referenced to the Topex/Poseidon ellipsoid. To make them comparable with the elevation models of this study, a conversion to the WGS84 ellipsoid was conducted by using Equation (1) [91].

$$h_{WGS84} = h_{Topex} - 0.707 \text{ m} \quad (1)$$

To detect outliers, e.g., from cloud reflections, all ICESat points with a height difference value greater than 60 m compared to the TanDEM-X heights were eliminated prior the evaluation. Finally, a total amount of around 450,000 points was used to evaluate the accuracy of the regional elevation models. Their locations are depicted in Figure 1. For the local elevation models an average amount of 500 elevation points was used for each scene. Scenes with less than 50 points were not evaluated in this study. Therefore, for 12 local DEMs no accuracy assessment with ICESat points was possible due to insufficient availability of elevation points.

3.3.2. ICESat-2

The Ice, Cloud, and land Elevation Satellite-2 (ICESat-2) was launched in September 2018 as the follow-on mission for ICESat [92,93]. It collects altimetry data from the Earth's surface with the Advanced Topographic Laser Altimeter System (ATLAS) instrument, which is a LiDAR system with a photon-level detection sensitivity. The outgoing single laser beam (532 nm) is split into three pairs of beams spaced approximately 3.3 km apart with a 90 m distance within the pairs. Furthermore, the laser emits a pulse signal every 0.7 m [93]. Therefore, it has a denser sampling and point coverage in comparison to its predecessor.

For accuracy assessment the measured terrain heights of the ATL03 and ATL08 version 001 products were used in this study. The ATL03 product contains height information of all received photons with a point density of 0.7 m along each track. All heights of the ATL08 dataset are processed in fixed 100 m data points along track, which contain at least 50 signal photons. They include the best fit terrain elevation of each 100 m segment calculated by interpolating all photons within the segment. Only few studies about the accuracy of these datasets are available yet. The terrain height accuracy of the ATL08 best fit dataset was denoted with a RMSE of 0.82 m for a large region in Finland [94].

Prior to the accuracy assessment, all points in both datasets were eliminated, which differ more than 30 m from TanDEM-X 12 m DEM heights. In this study a total of around 400,000 points were used from the ATL03 dataset and of around 650,000 points from the ATL08 dataset to evaluate the accuracy of the regional elevation models (Figure 1). For each local DEM between 800 and 270,000 additional ATL03 points were used for evaluation. From the ATL08 dataset an average amount of 500 height points were used to evaluate each scene. The datasets were already provided with WGS84 horizontal and WGS84 ellipsoidal vertical datum. Therefore, no further georeferencing was required for this study.

3.3.3. Very High-Resolution DEMs Derived by Unmanned Aerial Vehicle (UAV)

To evaluate the accuracy of the DEMs for large scale terrain, the height accuracy was compared to 19 elevation models derived with UAV-based photogrammetry with very high resolution. Figure 2 gives an overview about the covered terrain by these DEMs. They were achieved by imagery captured with two different systems. First, a 12 megapixel FC330 camera and a 20 mm full frame equivalent lens, fixed by a shock-absorbent gimbal on a rotary-wing quadcopter (type: DJI Phantom 4), set to capture images every 10 secs. Camera was set to shutter speed priority (1/1000) with ISO-100. Second, an octocopter (type: Mikrokopter MK-Easy) with a 36.4 MP full-format Sony Alpha 7R with a Sony 28mm lens (type: SEL28f20) was applied.

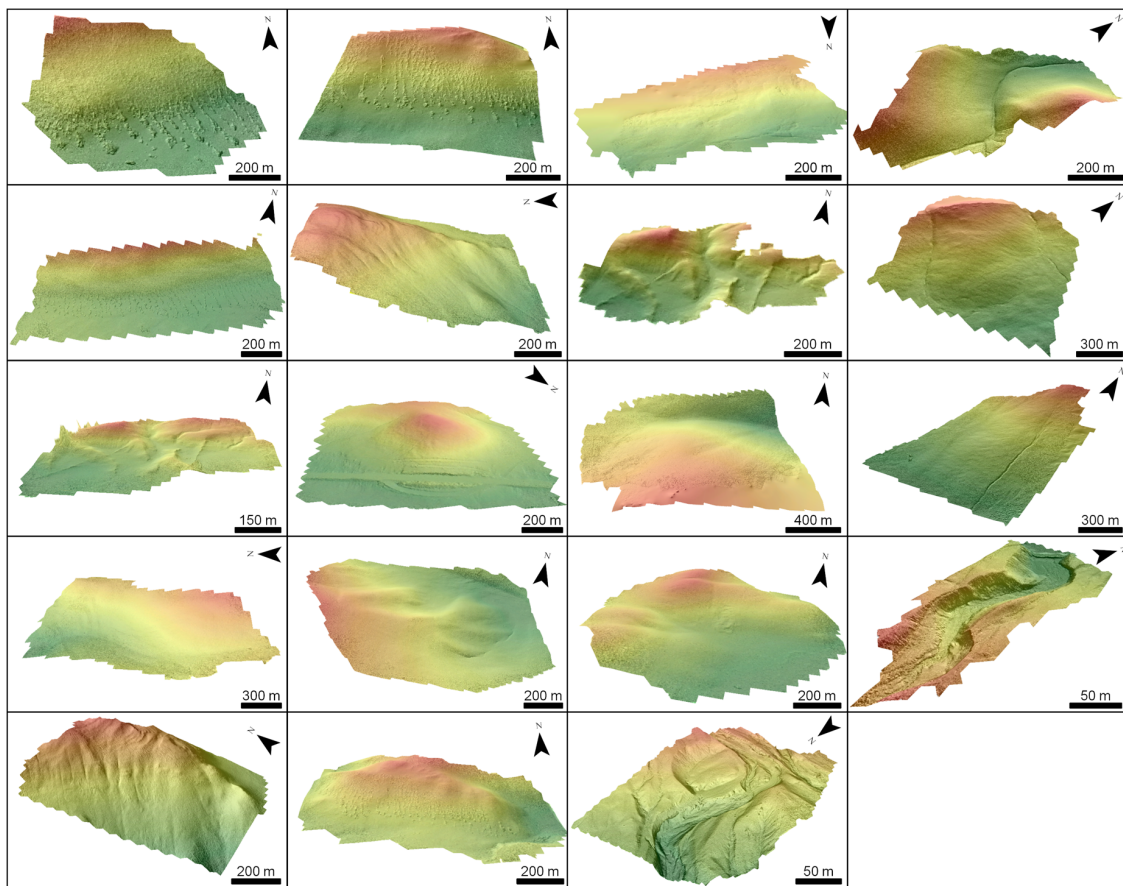


Figure 2. Perspective view of the covered relief of the 19 unmanned aerial vehicle (UAV) digital elevation models. Depicted relative altitudes of the raster datasets are from low (green) to high (red).

Flights at all sites were manually conducted between 10 am and 12 am local time on cloud-free days in a line-based pattern at two different heights, flying slower than 2.5 ms^{-1} to improve the accuracy of planimetry and altitude. Missions result in a high overlap of > 9 images per point. Subsequent image processing was conducted with Agisoft Photoscan Professional (vers. 1.4.2). Images were mostly aligned using evenly distributed GCPs measured by Real-Time Kinematic (RTK) positioning (type: Topcon GR5) and at 7 sites the direct Global Positioning System (GPS) measurements of the UAV recorded for each image were used. Processing in ultra-high quality for the dense point cloud generation resulted in a GSD of 1 cm to 8 cm for the DEM and each scene covers an average area of ca. 0.04 km^2 . Average errors range from 3 cm to 1.5 m for the datasets without GCPs in the horizontal direction and 3 cm to 1 m in the vertical direction. All data was exported in WGS84 UTM Zone 19S (EPSG: 32719).

To evaluate the vertical accuracy of all DEMs their GSD was up-sampled to the resolution of the UAV elevation models. Then pixel-wise errors were derived by subtracting the heights of UAV derived DEMs from the other elevation models.

3.3.4. Terrestrial Laser Scanning

The topography at several areas (see Figure 1) was recorded by a terrestrial laser scanner (type: Riegl VZ-2000) in combination with the same RTK positioning system (type: Topcon GR5) for registration of the final point cloud. The derived raw point clouds were filtered and afterwards interpolated by inverse distance weighting to a raster dataset with a 50 cm cell size in ArcGIS Pro 2.2.4 (Environmental Systems Research Institute) for the estimation of the statistics comparable to the other analyses. The covered terrain of these raster datasets is depicted in Figure 3. In addition, subsampled

point clouds with a similar mean point distance were compared with raster-datasets in CloudCompare and analyzed by the M3C2 algorithm in order to calculate detailed, reliable differences [95].

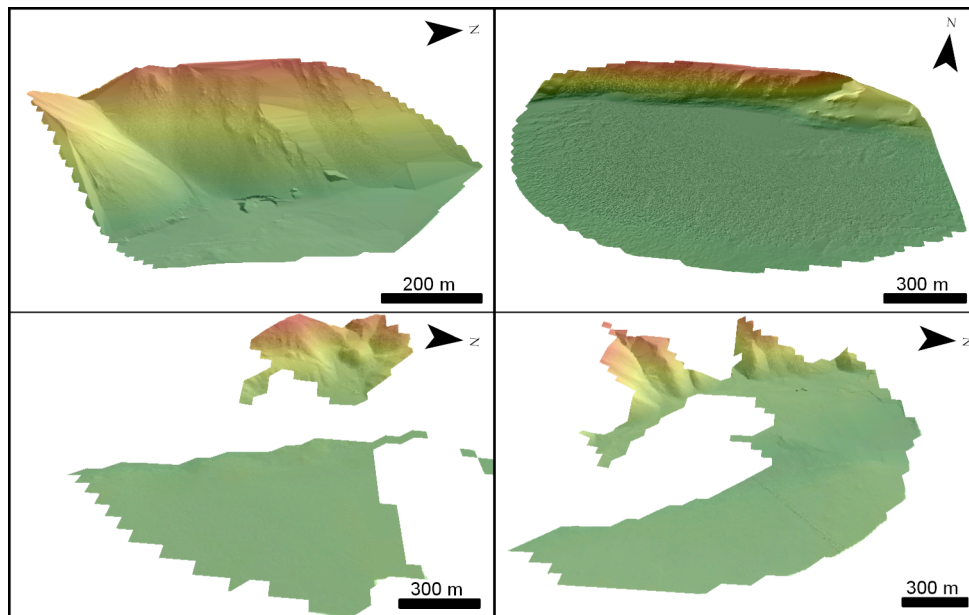


Figure 3. Perspective view of the covered relief of the four terrestrial laser scanning (TLS)-derived elevation raster datasets. Depicted relative altitudes of the raster datasets are from low (green) to high (red).

3.4. Accuracy Assessment

To assess the quality of the digital elevation models the deviation of height differences was calculated against all previously presented datasets. At first, the root mean square error for all digital elevation models compared to each available ground truth dataset was calculated from height differences with the following equation:

$$RMSE = \sqrt{\frac{\sum_{i=1}^n (\Delta h_i)^2}{n}} \quad (2)$$

where Δh_i = elevation difference between assessed DEM and reference DEM.

n = number of pixels.

Additionally, the normalized median absolute deviation was conducted, as height differences tend to be not normal distributed and this is a more robust measure against outliers [96]. The equation is:

$$NMAD = 1.4826 \times median(|\Delta h_i - m_{\Delta h}|) \quad (3)$$

where Δh_i = elevation difference between assessed DEM and reference DEM.

$m_{\Delta h}$ = median of all elevation differences.

If error values are normally distributed, the NMAD is identical to the RMSE, otherwise the RMSE will be larger than the NMAD.

Accuracy values are only comparable, if they can be related to the existing relief, since it is evident that different landscapes affect the accurateness of DEMs [42]. Therefore, a relief-adjusted evaluation of the ICESat heights was conducted by relating the accuracy of digital elevation models to specific terrain characteristics. In order to achieve this, several terrain parameters were calculated. First, the TRI was computed and divided into seven classes after Riley et al. [97] from leveled surfaces to extremely rugged terrain. Second, the slope was calculated and classified into five classes from flat ($<5^\circ$), gentle

(5° – 15°), moderate (15° – 25°), steep (25° – 35°) to extreme ($>35^{\circ}$). Additionally, the TPI after Weiss [98] was computed to assign the height errors to specific landforms. The number of classes was reduced to seven by combining the three ridge classes and two drainage classes to one class each. The TPI evaluation was only conducted for all global available datasets, as the coverage region of the others was too small to gain enough evaluation data for all classes. All landforms and terrain features were derived over the whole region on the basis of the 12 m TanDEM-X elevation model (see Figure 4).

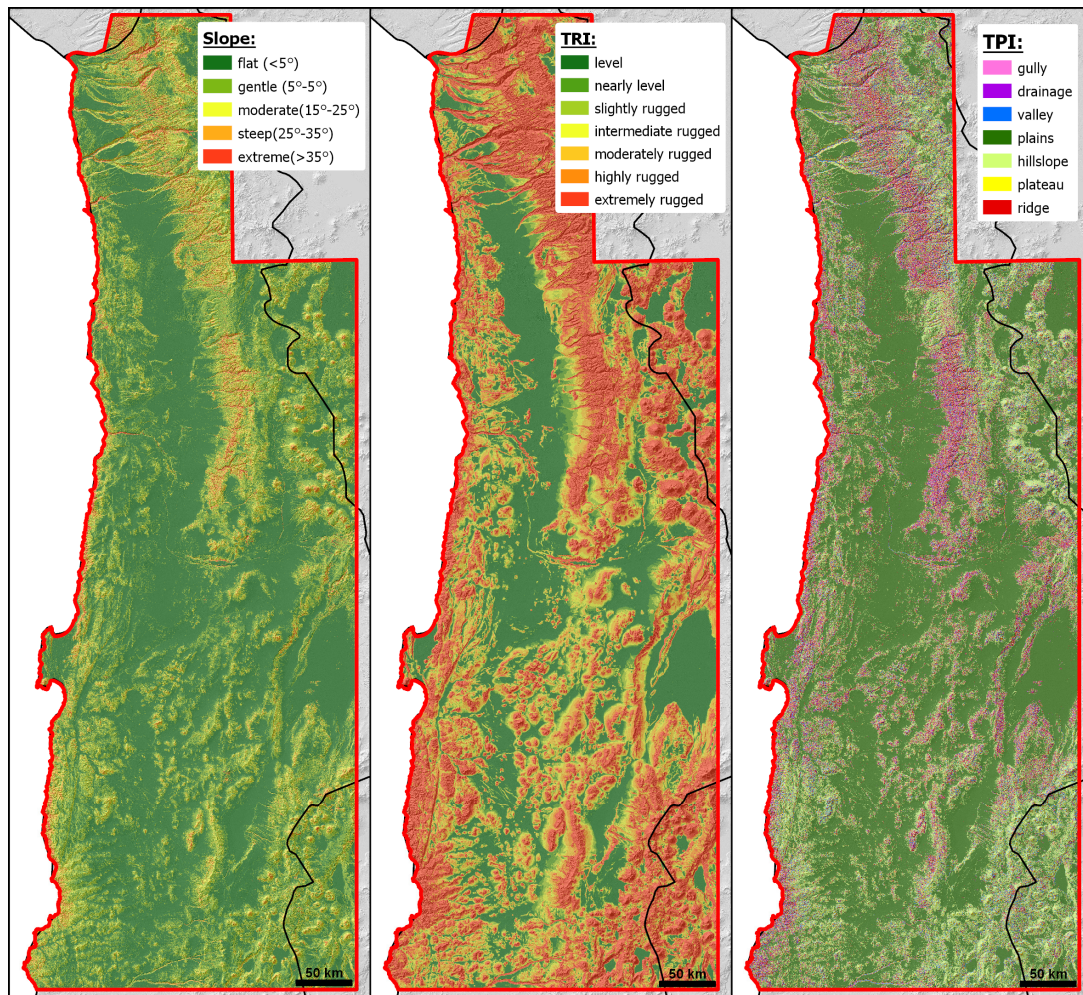


Figure 4. Spatial distribution of extracted terrain features slope, terrain ruggedness index (TRI) and topographic position index (TPI). Map is based on SRTM elevation data.

4. Results

4.1. Overall Accuracies

All determined overall accuracies are presented in Table A1 of Appendix A and Figure 5. Mostly, they show similar results for each dataset compared to all reference data. The ICESat-2 ATL08 dataset generally produced the highest error values for the DEMs in comparison to the other reference datasets. For the TanDEM-X 90 m and the SPOT 125 datasets in particular, a very high RMSE (13.9 m and 11.6 m) was calculated. Overall, for 17 DEMs the highest RMSE and for 21 DEMs the highest NMAD values were calculated with the ICESat-2 ATL08 dataset. For the UAV data, the lowest differences between RMSE and NMAD values can be observed for most datasets in comparison to all ICESat and TLS datasets. While the mean difference between RMSE and NMAD values is 0.4 m for the UAV dataset, it is more than 1.7 m for the other datasets. The highest differences between RMSE and NMAD can be observed for the TLS point cloud dataset with a mean difference of 4.8 m.

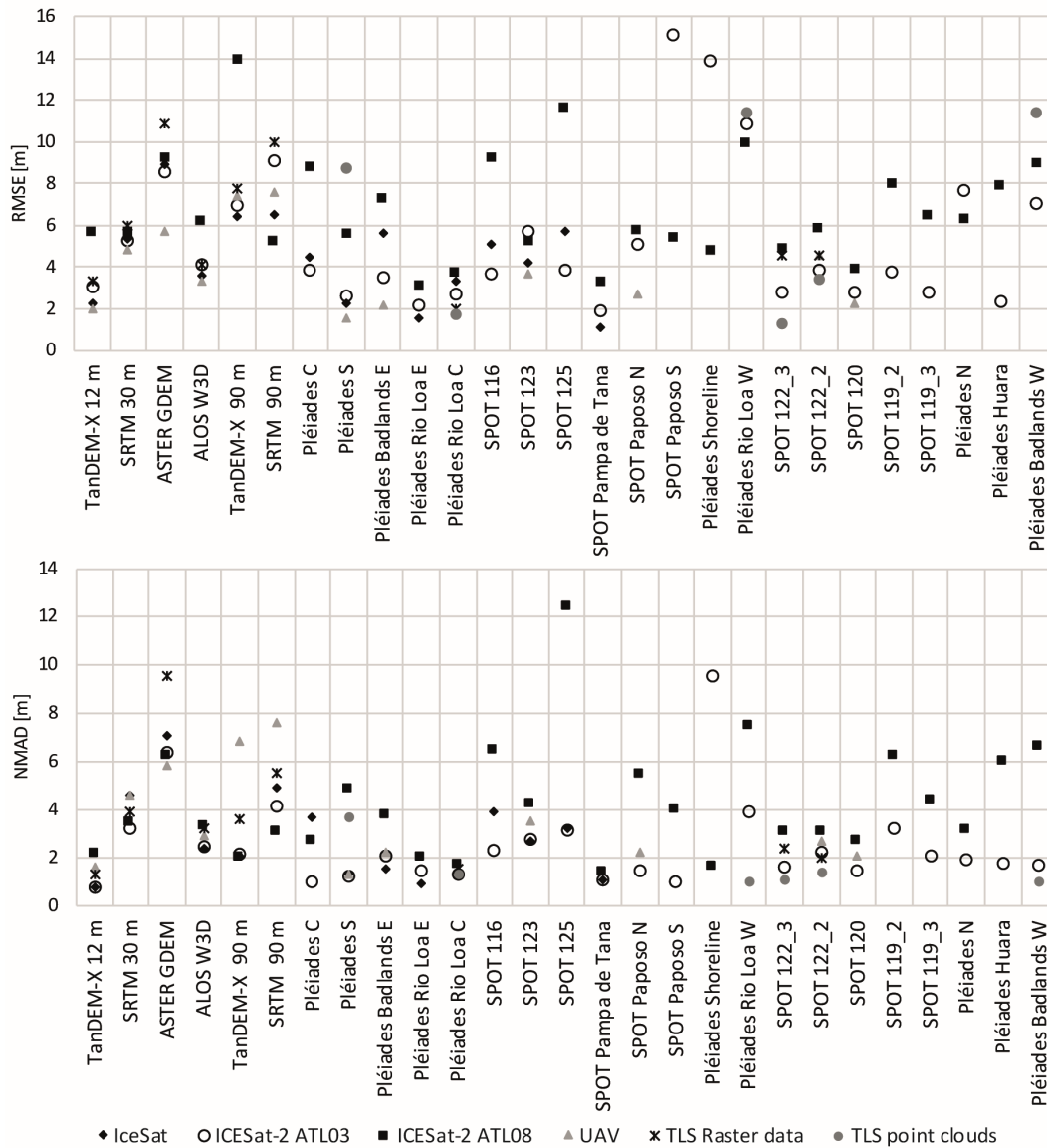


Figure 5. Comparison of all calculated overall accuracies for each digital elevation model.

For all global DEMs, the lowest RMSE and NMAD values are detectable for the TanDEM-X 12 m dataset. The highest RMSE of 5.7 m was calculated for TanDEM-X with the ICESat-2 ATL08 dataset, the lowest with the UAV dataset (2.0 m). The NMAD is generally lower with values between 0.8 m and 2.2 m. The calculated accuracy values for the ALOS W3D dataset are slightly higher with a RMSE between 3.3 m and 6.2 m and a NMAD between 2.4 m and 3.3 m. Thus, the ALOS accuracies are higher in comparison to the other 30 m datasets.

The lowest accuracies were detected for the 30 m ASTER GDEM, which also tend to be lower than the calculated accuracies of both DEMs with 90 m GSD. The calculated RMSEs for the ASTER GDEM V3 are between 5.7 m and 10.9 m and the NMAD ranges between 5.8 m and 9.5 m. The smallest differences between RMSE and NMAD are detectable for the SRTM 30 m dataset, with a relatively small range between 4.8 m and 6.0 m (RMSE) and 3.2 m and 4.6 m (NMAD).

In contrast, for the 90 m TanDEM-X it is noticeable that the discrepancy between the calculated RMSE and NMAD values are rather high, especially for all three ICESat datasets. The RMSE ranges between 6.4 m and 13.9 m, the calculated NMAD between 2.0 m and 6.8 m. Thus, the NMAD values are generally lower compared to the 90 m SRTM which are between 3.0 m and 7.6 m. The calculated RMSEs of the SRTM 90 m dataset are on a similar level with values between 5.2 m and 10.1 m.

The results of the local scaled DEMs, derived by Pléiades and SPOT imagery, showed the highest overall accuracies for the SPOT-based Pampa de Tana scene with a RMSE between 1.1 m and 3.3 m. The calculated NMAD values for this dataset range between 1.1 m and 1.4 m. For the majority of the local DEMs the calculated RMSE ranges between 2.0 m and 4.0 m and the NMAD between 1.0 m and 3.0 m. Relatively high RMSE values were calculated for the Pléiades Rio Loa W (9.9–11.4 m) and Badlands W (7.1–11.4 m) datasets. The SPOT Paposo S (15.1 m) and Pléiades Shoreline (13.9 m) datasets also achieve very high RMSE values for the ICESat-2 ATL03 dataset. While for the Pléiades Shoreline dataset the NMAD is also very high with 9.6 m, it is extremely low (1.0 m) for the SPOT Paposo S DEM. Compared to the ICESat-2 ATL08 reference data, the results show for the SPOT 125 DEM the highest error values with 11.6 m (RMSE) and 12.3 m (NMAD). However, the error values for this dataset are significantly lower in comparison with the ICESat (RMSE: 5.7 m; NMAD: 3.2 m) and ICESat-2 ATL03 (RMSE: 3.9 m; NMAD: 3.2 m) dataset. For the Pléiades S DEM a relatively high RMSE error was measured with the TLS point cloud data (RMSE: 8.7 m), whereas it is generally lower for all other reference datasets.

4.2. Terrain-Dependent Accuracies

The results depicted in Figure 6 show the RMSE and NMAD of all digital elevation models calculated with the ICESat reference dataset according to their terrain ruggedness index. The calculation of error values was conducted here only for corresponding datasets with at least 10 available elevation points for more than one class. All other datasets were not considered.

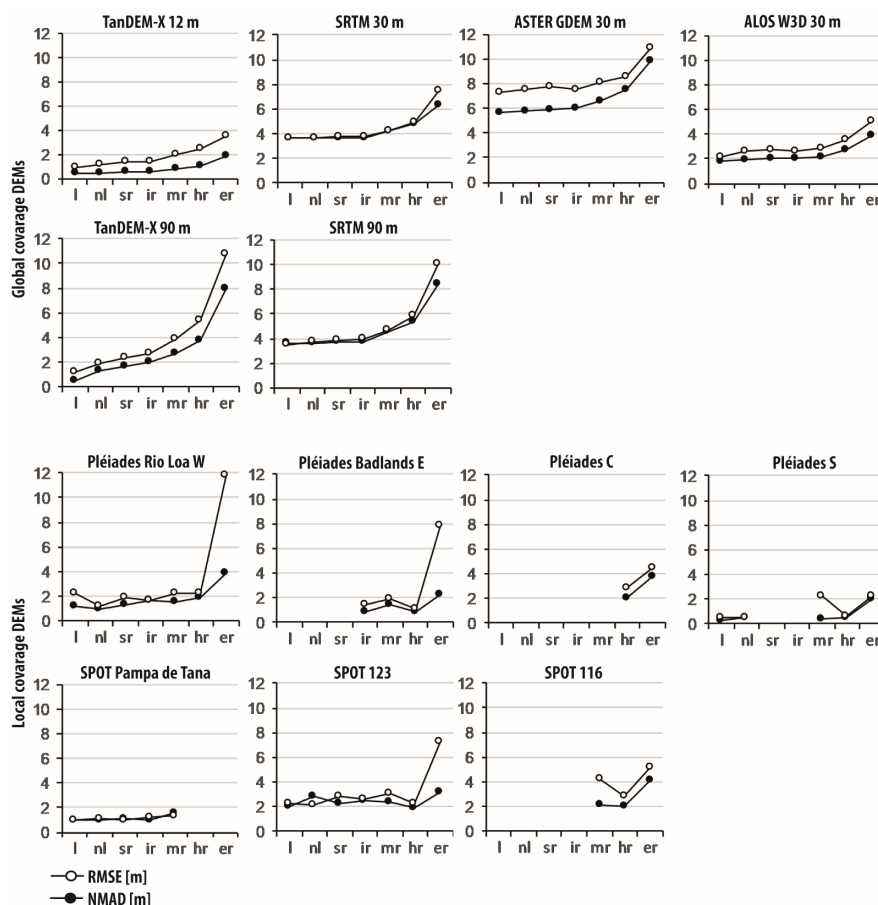


Figure 6. Calculated root mean squared error (RMSE) of elevation differences according to the classified terrain ruggedness index from level to extremely rugged. Categorization of classes was conducted after Riley et al. (1999). Classes are level (l), nearly level (nl), slightly rugged (sr), intermediate rugged (ir), moderately rugged (mr), highly rugged (hr), extremely rugged (er).

The diagram shows for most elevation models only a slight increase of error from class ‘level’ to class ‘highly rugged’. Both DEMs with a 90 m GSD have a higher increase of uncertainty from class ‘intermediate rugged’ terrain to ‘extremely rugged’ terrain. For all elevation models the biggest loss in accuracy is visible in the category ‘extremely rugged’. The 90 m TanDEM-X in particular shows a very high accuracy in leveled terrain, which is similar to the 12 m TanDEM-X, but in rough terrain the accuracy decreases more than for all other DEMs and is even lower than for the SRTM 90 m DEM in ‘extremely rugged’ terrain. The freely available ALOS W3D dataset shows a better overall accuracy and terrain independency, than the other 30 m DEMs. Lowest accuracies were detected for the 30 m ASTER GDEM. Only in category ‘extremely rugged’ the 90 m TanDEM-X and 90 m SRTM perform with similar error values.

The highest accuracies according to their terrain ruggedness were detected for the high resolution Pléiades S DEM both in flat and rough terrain. For the Pléiades Rio Loa W and Pléiades Badlands E DEMs a strong increase of RMSE is detectable in the category ‘extremely rugged’, whereas the RMSE is rather low for these DEMs in all other categories. Furthermore, the NMAD of these two elevation models in the highest category is also rather low and does not show such an increase of error.

Figure 7 shows the RMSE and NMAD of all elevation models according to their slope. All values were calculated against the ICESat reference dataset and only datasets with at least two classes with more than 10 reference points are considered here. Similar to the results of TRI classes an increase of RMSE and NMAD values for steeper slopes is observable here. For DEMs with lower GSD a stronger decrease of accuracy is detectable for rising slope degrees. Thus, the results show for the 90 m SRTM (RMSE: 20.6 m, NMAD 19.6 m) and the 90 m TanDEM-X (RMSE: 22.2 m, NMAD 21.0 m) the highest drop of accuracies in steep slope terrain.

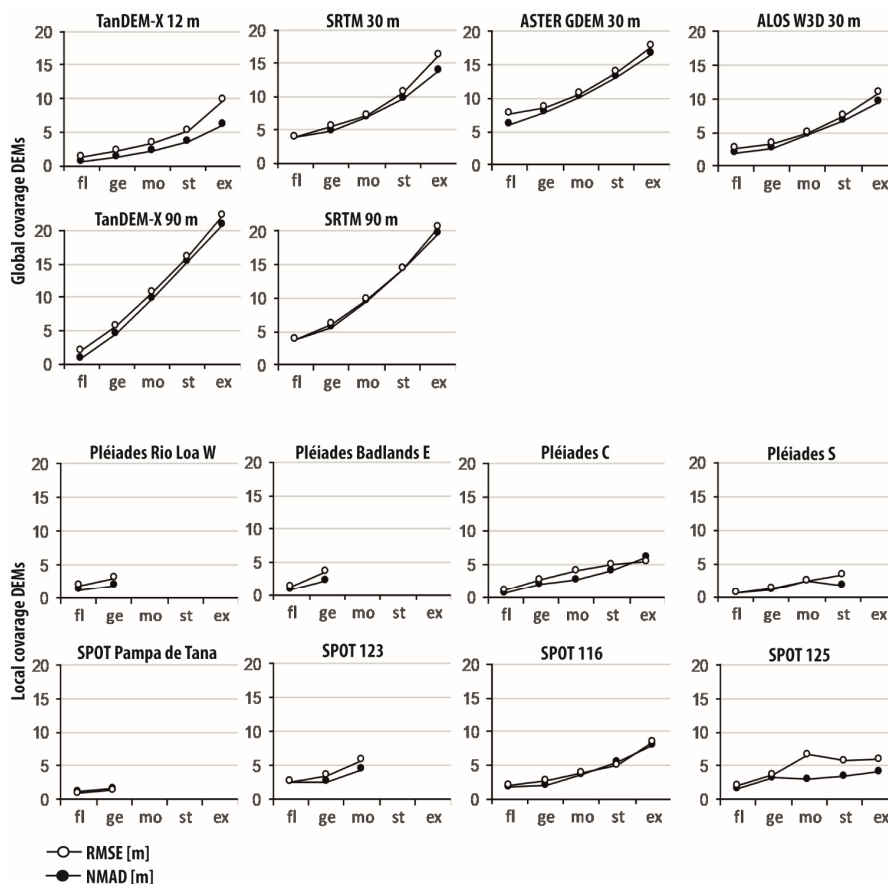


Figure 7. Calculated RMSE and normalized median absolute deviation (NMAD) of elevation differences according to the slope. Derived slope classes are flat (fl), gentle (ge), moderate (mo), steep (st) and extreme (ex).

Generally, the local DEMs derived from Pléiades and SPOT scenes achieved the highest accuracy values. Though, the diagram curves indicate a slightly higher accuracy for Pléiades datasets compared to SPOT scenes. For very steep slopes only the TanDEM-X with a GSD of 12 m is able to achieve similar accuracy values (RMSE: 9.7 m, NMAD: 6.0 m) compared to the very high-resolution DEMs, which have an average accuracy of RMSE 6.6 m and NMAD of 6.1 m here.

Figure 8 depicts the RMSE and NMAD for all global available DEMs according to their respective TPI landform class. The results show for all elevation models the lowest RMSE and NMAD values for the class ‘plains’. All other classes achieved significantly lower accuracies. The highest error values were determined for the landform classes ‘gully’, ‘drainage’ and ‘ridge’.

The highest accuracies are calculated for the 12 m TanDEM-X, which has also the lowest error values for class ‘plains’ (RMSE: 1.0 m, NMAD: 1.1 m) and the highest RMSE for class ‘drainage’ with 5.0 m. For the NMAD calculation the highest error values are determined for the classes ‘gully’ and ‘drainage’ with 2.4 m.

Again, in comparison to the other 30 m DEMs the ALOS W3D achieved higher accuracies between 2.4 m (RMSE) and 1.8 m (NMAD) for class ‘plains’ and 6.1 m (RMSE) and 4.8 m (NMAD) for classes ‘gully’ and ‘drainage’. The lowest accuracies are generally measured for the 30 m ASTER GDEM with values between 7.6 m (RMSE) and 5.9 m (NMAD) for class ‘plains’ and 11.4 m (RMSE) and 9.8 m (NMAD) for class ‘gully’. Only the calculated RMSE for the 90 m TanDEM-X DEM was even higher for the classes ‘gully’, ‘drainage’ and ‘ridge’ with values of 11.7 m, 12.2 m and 11.3 m. The highest NMAD values are calculated for the ASTER GDEM in all classes. The biggest differences in accuracy are also observable here for the 90 m TanDEM-X elevation model. Whereas its error values are very low for class ‘plains’ (RMSE: 1.7 m, NMAD: 0.9 m), these rise significantly for all other classes.

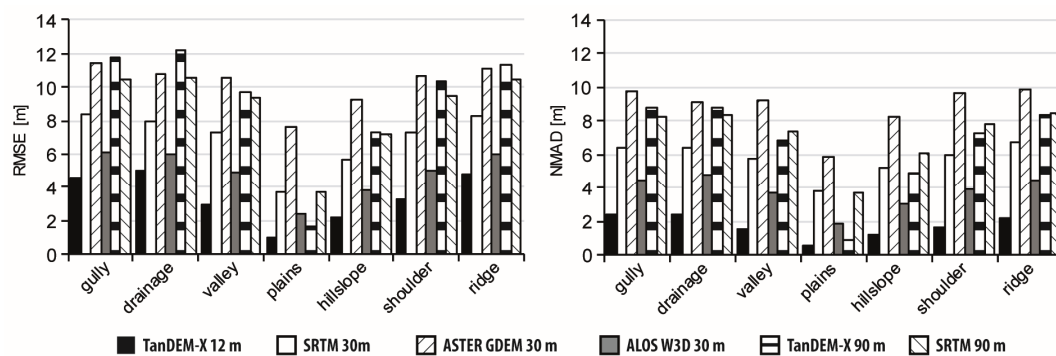


Figure 8. Calculated RMSE and NMAD of elevation according to topographic position index (TPI) classes classified with 12 m TanDEM-X.

4.3. Local-Scale Evaluation

Figure 9 depicts the distribution of errors of each individual UAV scene. The results show for both RMSE and NMAD that the deviations between the different UAV scenes rise for elevation models with coarser GSDs. Thus, the highest range is measured for the TanDEM-X 90 m elevation models with calculated RMSE values between 4.4 m and 11.2 m. NMAD values range from 2.8 m to 10.9 m. In contrast, the differences for the TanDEM-X 12 m DEM only range between 1.0 m and 4.6 m (RMSE) and 0.9 m and 3.0 m (NMAD). For the ALOS DEM, also relatively low variations are detectable with RMSEs from 2.1 m to 5.1 m and NMAD values from 1.6 m to 4.2 m.

For the very high-resolution Pleiades and SPOT scenes varying differences are observable. Especially for SPOT Pajoso N the results show relatively large differences, which are greater than the differences of TanDEM-X 12 m and ALOS W3D. For SPOT 120 and Pléiades S almost no deviation of the results was measured.

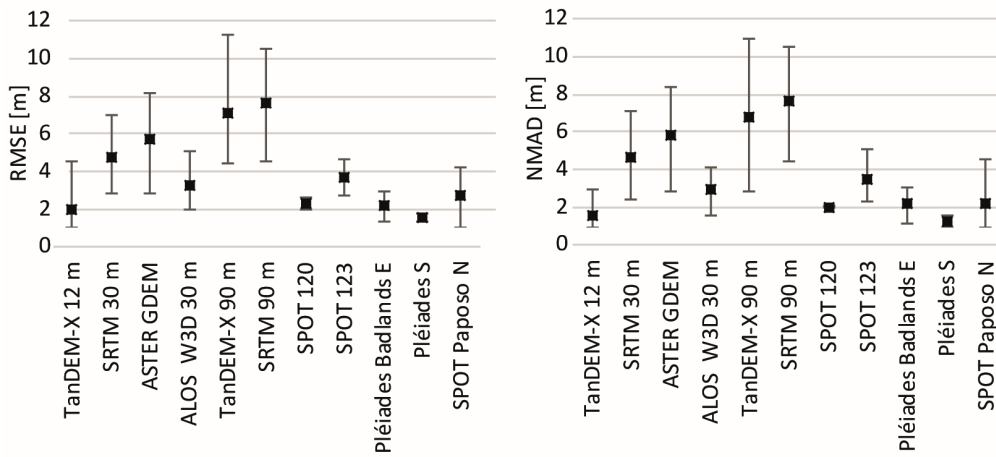


Figure 9. Distribution of calculated RMSE and NMAD of the individual UAV-derived reference datasets compared to elevation models.

A visual interpretation on a local scale shows that height differences are mainly affected by small scale landforms with large height differences on small areas. It is depicted in Figure 10 for two example sites that DEM heights in depressions tend to be higher than the heights of the reference elevation data. In contrast, the heights of ridges and summits tend to be lower in comparison to reference data. It can be observed that this effect is increased for the TanDEM-X 12 m DEM compared to the 5 m Pléiades S elevation model. All DEMs with a coarser GSD were not at all able to depict the sample canyons in a sufficient way.

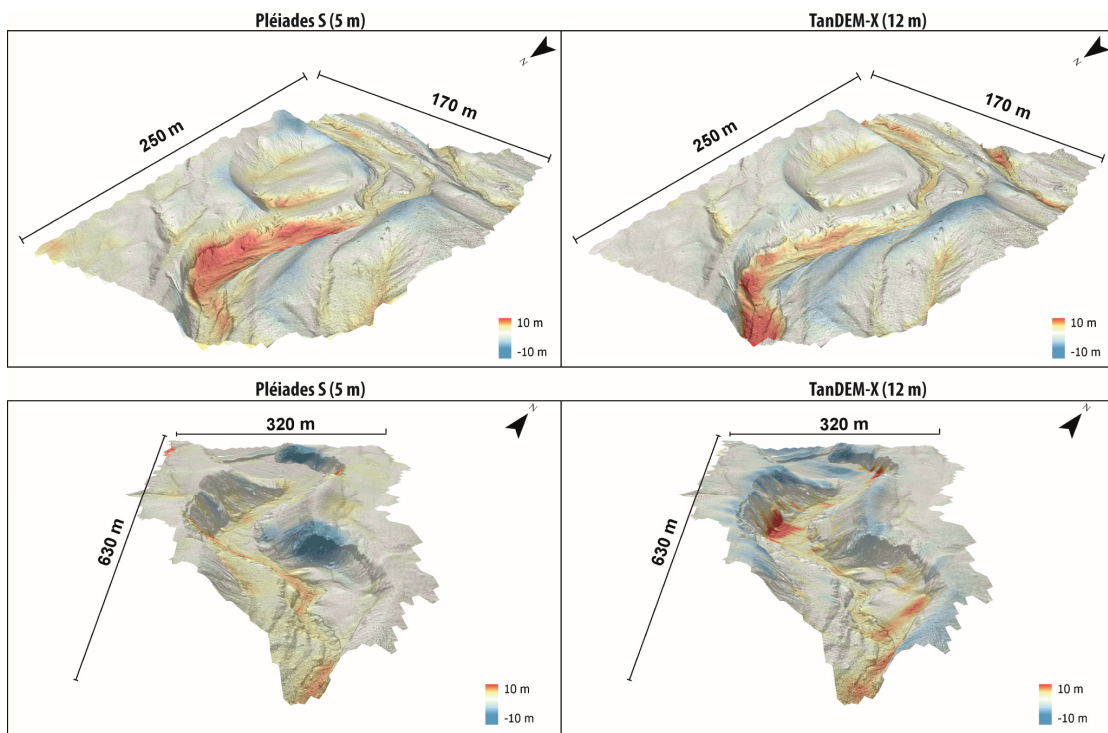


Figure 10. Spatial distribution of elevation differences of Pléiades S and TanDEM-X 12 m data compared to UAV reference data at two different sites. Pléiades satellite imagery data: © CNES (2016), Distribution Airbus DS. TanDEM-X World WorldDEM™ data: © DLR (2017).

5. Discussion

The overall accuracies of the global DEMs achieved are within the expected range when comparing them with findings from other studies. As the relief of the study area represents a cross section of flat to very steep landscapes, the overall accuracies can be taken as an average error value over a broad landscape. Thus, the achieved overall accuracies are lower than conducted by studies in mostly flat terrain [26,45,56,58]. However, the results of these studies mostly fit well with the achieved results in flat landscapes. Likewise, the calculated overall accuracies in this study are generally higher than findings from many studies with predominantly undulated to very steep terrain conditions [51,55,57,61]. Nevertheless, these results are also consistent to the calculated error values in very steep terrain.

Of all globally available elevation datasets only the 12 m TanDEM-X was able to achieve similar accuracies in comparison to the local DEMs derived from Pléiades and SPOT imagery. Also, small-scale analyses show that this DEM is able to depict most terrain features compared to the other global DEMs. The results are generally consistent with findings of other studies, which also showed that the accuracy of the new TanDEM-X generally outperforms the accuracy of ASTER GDEM and SRTM [56,58–60]. Only the freely available ALOS W3D dataset was able to achieve similar results with only slightly lower overall accuracies. In comparison of all 30 m DEMs the ALOS W3D seems to be superior compared to SRTM and ASTER. Therefore, similar findings from other studies can be agreed here [50,99]. It shows a good agreement with both evaluation scales and is more stable over all terrain types, slopes and landforms, only slightly worse than the TanDEM-X 12 m dataset. In mountainous areas with steep slopes in particular, the performance of ALOS W3D seems to be far superior compared to the other 30 m elevation models. This is probably caused by the fact that it is resampled from a higher resolution dataset and still more terrain features remain in the 30 m elevation data. Furthermore, optical imagery is often less affected by relief distortions due to usually small viewing angles. Nevertheless, the goal of 5 m vertical accuracy for ALOS W3D can only be reached here in flat to undulated terrain. In very steep terrain the uncertainties are still higher.

Possibly, the high accuracy values of TanDEM-X and ALOS W3D compared to the ICESat dataset are affected by the fact that ICESat points were already used for quality assessments during the generation process of both elevation models [100–102]. Thus, some correlation between those DEMs and the evaluation dataset cannot be excluded. However, the results of the evaluation with completely independent elevation data from UAV and TLS measurements produced similar results and a significant positive influence of ICESat data on the accuracy of both DEMs cannot be observed here.

The ASTER GDEM achieved the lowest overall accuracies in comparison to all global datasets. Furthermore, except for very steep terrain, its accuracies seem to be lower than the accuracies of both 90 m DEMs. Numerous studies showed that the previous 2nd version of the ASTER GDEM achieved the least accurate terrain representation compared to other freely available DEMs [41,43,103,104]. Although a direct comparison of the latest two ASTER GDEM Versions was not conducted here, the results indicate that also the last update of ASTER GDEM is not able to achieve the accuracies of the other global elevation datasets.

For all DEMs, a decrease in accuracy in rougher terrain compared to flat landscapes can be observed. This effect is particularly stronger for elevation models with coarser GSD, which have a higher decrease in accuracy compared to high-resolution elevation models. For the 90 m TanDEM-X in particular, which is similarly accurate in flat terrain than the 12 m TanDEM-X elevation model, a very high drop in accuracy can be observed in rougher terrain with steep slopes. A similar trend was also observable for the SRTM 90 m DEM but the decrease in accuracy is even higher for the 90 m TanDEM-X. This is in accordance with findings of Altunel [47], who already noticed some overestimations of 90 m TanDEM-X for cliffy terrain and a high accuracy in flat areas. Generally, a comparison of the two 90 m elevation datasets leads to the conclusion that TanDEM-X is significantly more accurate in flat landscapes, but the SRTM 90 m still seems advantageous in steeper relief. Furthermore, the difference between the calculated RMSE and NMAD is conspicuously high for the TanDEM-X 90 m dataset. It can be assumed that more outliers exist in these DEM in its first version compared to the

other global elevation models, which were already revised several times. Nevertheless, the results lead to the conclusion that both DEMs with 90 m GSD are not suitable for accurate large scale terrain analyses, especially in rough landscapes. Likewise, the results of the ASTER GDEM show that the accuracy of this DEM is already lower in flat landscapes than the accuracy of high-resolution DEMs in rough terrain. Thus, for this DEMs the results indicate a least suitability for geomorphometric analyses in this area.

The results for the local DEMs derived from stereo satellite imagery show a varying overall accuracy, which highly depends on the topography of each scene. Relating them to slope or TRI tends in most cases to lower error values for each terrain category compared to the globally available elevation models. Furthermore, the accuracies of Pléiades imagery seem to be slightly higher than images derived from SPOT imagery.

For most DEMs similar accuracy values could be achieved by the different reference datasets. However, for some DEMs some anomalies could be detected. For example, the Pléiades S scene achieved relative low accuracies compared to the TLS point clouds, whereas the values were significantly lower for all other datasets. This is mainly caused by different locations of the reference datasets, even in this small area. While all ICESat datasets and the UAV data mostly cover flatter areas, the TLS data is situated on a hillside with relative steep slopes. Therefore, it can be assumed, that also for this DEM the error values are much higher in steeper areas compared to flatter landscapes. Also, the relatively high error values for the Pléiades Rio Loa W and Pléiades Badlands W DEMs can be explained with very steep relief conditions. Both scenes and the evaluation data cover the Rio Loa canyon which is extremely steep at this point with average slope angles of more than 30°. This steepness possibly produces more outliers, which are represented in the RMSE values, whereas the NMAD values are much lower.

In contrast, the large differences in the overall accuracy results from the Pléiades Shoreline DEM with the ICESat-2 ATL03 and ATL08 reference data cannot be explained here by the relief, as both point datasets cover the same track. Therefore, it can be supposed, that these differences are originated in the reference dataset. A similar contradiction is also evident in the results of the SPOT Paposo S DEM. Indeed, in contrast to the results of the Pléiades Shoreline DEM there is also a large difference between the ICESat-2 ATL03 RMSE and NMAD. While the RMSE is with 15.1 m very high, the NMAD is extremely low with 1.0 m. This possibly indicates that a great amount of outliers exists in the ICESat-2 ATL03 dataset at this location.

It is conspicuous that for most DEMs the highest values were calculated by the ICESat-2 ATL08 dataset, which are often not in line with the error values calculated with other datasets. It can be assumed that the interpolated ATL08 heights are probably less suitable for DEM accuracy assessment. Thus, it is likely that the calculated values by the ATL08 dataset at this early stage overestimate the error of the DEMs. In contrast, the ICESat-2 ATL03 mostly fit well with the results from the other reference datasets.

The TLS raster data produced higher error values than the point clouds from TLS measurements. This is possibly caused by the height interpolations of some areas, which were not covered during the measurement process. During the generation process, it was not completely possible to exclude all of these areas and some small areas with probably lower accuracy remained for the evaluation process.

A comparison of elevation differences on a local scale shows, that the heights of small incised canyons are overestimated at the bottom and underestimated at upper elevations. The results reveal, that even for the very high-resolution DEMs a slight decrease in the deepness of such a canyon is detectable. This lack of deepness rises with coarser resolutions.

6. Conclusions

In this contribution, the accuracy of a multitude of digital elevation models was evaluated against various reference datasets. Furthermore, the influence of terrain on the accuracy of these DEMs was analyzed by relating the accuracy values to several extracted terrain features and landforms on a

regional scale. The results reveal that the rougher and steeper the landscape is the higher resolutions are necessary to depict the landscape in an accurate way. For instance, the 90 m TanDEM-X elevation model showed eight times higher RMSE error values in terrain with steep slopes (25–35°) compared to landscapes with flat slopes (0–5°). Thus, an average rise of about 5 m RMSE per 10° slope can be assumed for this DEM. In contrast, for the 12 m TanDEM-X the increase of error in steep terrain (25–35°) is only four times as high as in flat landscapes with slopes less than 5° and an average rise of 1.5 m RMSE per 10° slope can be supposed here. The results of the very high resolution DEMs from Pléiades and SPOT satellites reveal that the RMSE error is increasing by about 1 m per 10° slope. Therefore, in an increase of error by about three times in terrain with steep slopes compared to flat landscapes could be expected for these DEMs. Hence, for analyses in flatter landscapes a 30 m or 90 m DEM could possibly be sufficient. If the relief is steeper, only high-resolution DEMs show satisfying accuracies. This applies for a regional coverage, but even more for analyses on a local scale with smaller landforms. Furthermore, the presented results are valid for regions with almost no vegetation cover. It cannot be stated here how the accuracies of different DEMs are affected by vegetation and to which degree an increase of error is probably detectable in dense vegetated areas.

The results of this study point out that of all globally available datasets only the TanDEM-X 12 m and partly the 30 m ALOS World 3D are able to depict the landscape in the same accuracy as very high resolution DEMs with a GSD of 5 m. Thus, it can be assumed that the 12 m TanDEM-X data are suitable not only for global scale analyses, but also has a sufficient accuracy for local scale analysis in flat to moderately sloped landscapes. Only in landscapes with very steep terrain they seem to be less accurate than DEMs derived by Pléiades and SPOT imagery. All other freely worldwide available elevation models were not able to achieve promising accuracies here and seem less suitable for delineating small terrain features in large scales.

Furthermore, it can be concluded that most reference datasets from different sources produced coherent values. Only the ICESat-2 ATL08 dataset seems to significantly underestimate the accuracy, especially of the local-scaled DEMs.

Author Contributions: Methodology, Formal Analysis, Visualization, T.K.; Conceptualization, Supervision, Funding Acquisition, D.H.; Validation, Data Curation, Writing—Original Draft Preparation, Writing—Review and Editing, T.K. and D.H.

Funding: This research was funded by the Deutsche Forschungsgemeinschaft (DFG, German Research Foundation)—Projektnummer 268236062—SFB 1211.

Acknowledgments: The TanDEM-X WorldDEM™ data is provided by a DLR Science grant, 2017. Pléiades satellite imagery data: © CNES (2014–2016), distributed by Airbus DS. SPOT 6 and 7 imagery data: ©Airbus DS (2013–2017). We thank both anonymous reviewers for improving the contribution.

Conflicts of Interest: The authors declare no conflict of interest.

Appendix A

Table A1. Overall accuracies of all digital elevation models compared to the reference point datasets of Ice, Cloud and Land Elevation Satellite (ICESat), ICESat-2 ATL03, ICESat-2 ATL08 and Terrestrial Laser Scanning (TLS) point clouds as well as raster datasets derived from unmanned aerial vehicle (UAV)-based photogrammetry and TLS datasets. Listed are the ground sampling distance (GSD), the calculated root mean square error (RMSE), the normalized median absolute deviation (NMAD) and the total amount of applied points or raster for each DEM.

DEM	GSD	ICESat			ICESat-2 ATL03			ICESat-2 ATL08			UAV DEMs			TLS Raster Data			TLS Point Clouds		
		RMSE [m]	NMAD [m]	No. Points	RMSE [m]	NMAD [m]	No. Points	RMSE [m]	NMAD [m]	No. Points	RMSE [m]	NMAD [m]	No. Rasters	RMSE [m]	NMAD [m]	No. Rasters	RMSE [m]	NMAD [m]	No. Points
TanDEM-X	12m	2.3	0.8	453434	3.1	0.8	392333	5.7	2.2	643926	2.0	1.6	19	3.3	1.3	4	-	-	-
SRTM	30m	5.4	4.6	453434	5.3	3.2	392333	5.7	3.5	643926	4.8	4.6	19	6.0	3.9	4	-	-	-
ASTER GDEM	30m	8.9	7.1	453434	8.6	6.4	392333	9.2	6.2	643926	5.7	5.8	19	10.9	9.5	4	-	-	-
ALOS W3D	30m	3.6	2.4	447372	4.1	2.4	392043	6.2	3.3	636761	3.3	2.9	19	4.1	3.2	4	-	-	-
TanDEM -X	90m	6.4	2.1	453434	7.0	2.1	392333	13.9	2.0	643926	7.4	6.8	19	7.8	3.6	4	-	-	-
SRTM	90m	6.5	4.9	453434	9.1	4.1	392333	5.2	3.0	643926	7.6	7.6	19	10.0	5.5	4	-	-	-
Pléiades C	5m	4.5	3.7	629	3.9	1.0	11796	8.8	2.7	67	-	-	-	-	-	-	-	-	-
Pléiades S	5m	2.3	1.3	273	2.6	1.2	9852	5.6	4.8	154	1.6	1.3	2	-	-	-	8.7	3.6	1004405
Pléiades Badlands E	5m	5.6	1.5	158	3.5	2.1	12131	7.3	3.8	244	2.2	2.2	4	-	-	-	-	-	-
Pléiades Rio Loa E	5m	1.6	0.9	634	2.2	1.4	271078	3.1	2.0	1819	-	-	-	-	-	-	-	-	-
Pléiades Rio Loa C	5m	3.3	1.4	475	2.7	1.3	124934	3.7	1.7	1057	-	-	-	2.0	1.5	1	1.7	1.2	242730
SPOT 116	5m	5.1	3.9	1293	3.7	2.3	55427	9.2	6.5	614	-	-	-	-	-	-	-	-	-
SPOT 123	5m	4.2	2.7	424	5.7	2.8	34806	5.2	4.2	648	3.7	3.5	4	-	-	-	-	-	-
SPOT 125	5m	5.7	3.2	958	3.9	3.2	75149	11.6	12.3	388	-	-	-	-	-	-	-	-	-
SPOT Pampa de Tana	5m	1.1	1.1	445	1.9	1.1	67805	3.3	1.4	417	-	-	-	-	-	-	-	-	-
SPOT Paposo N	5m	-	-	-	5.1	1.5	143298	5.8	5.4	951	2.7	2.2	4	-	-	-	-	-	-
SPOT Paposo S	5m	-	-	-	15.1	1.0	2235	5.4	4.0	695	-	-	-	-	-	-	-	-	-
Pléiades Shoreline	5m	-	-	-	13.9	9.6	177271	4.8	1.6	294	-	-	-	-	-	-	-	-	-
Pléiades Rio Loa W	5m	-	-	-	10.9	3.9	4793	9.9	7.5	407	-	-	-	-	-	-	11.4	0.9	880609
SPOT 122_3	5m	-	-	-	2.8	1.6	26349	4.9	3.0	220	-	-	-	4.6	2.4	1	1.3	1.0	230017
SPOT 122_2	5m	-	-	-	3.9	2.2	68967	5.9	3.1	449	4.6	2.7	1	4.6	2.0	1	3.4	1.3	347589
SPOT 120	5m	-	-	-	2.8	1.4	66810	3.9	2.7	281	2.3	2.1	2	-	-	-	-	-	-
SPOT 119_2	5m	-	-	-	3.8	3.2	77527	8.0	6.2	599	-	-	-	-	-	-	-	-	-
SPOT 119_3	5m	-	-	-	2.8	2.0	52071	6.5	4.4	456	-	-	-	-	-	-	-	-	-
Pléiades N	5m	-	-	-	7.7	1.9	2551	6.3	3.1	200	-	-	-	-	-	-	-	-	-
Pléiades Huara	5m	-	-	-	2.4	1.7	73224	7.9	6.0	572	-	-	-	-	-	-	-	-	-
Pléiades Badlands W	5m	-	-	-	7.1	1.7	839	9.0	6.6	63	-	-	-	-	-	-	11.4	0.9	880609

References

1. Wilson, J.P. Digital terrain modeling. *Geomorphology* **2012**, *137*, 107–121. [[CrossRef](#)]
2. Farr, T.G.; Rosen, P.A.; Caro, E.; Crippen, R.; Duren, R.; Hensley, S.; Kobrick, M.; Paller, M.; Rodriguez, E.; Roth, L.; et al. The Shuttle Radar Topography Mission. *Rev. Geophys.* **2007**, *45*. [[CrossRef](#)]
3. Tachikawa, T.; Kaku, M.; Iwasaki, A.; Gesch, D.B.; Oimoen, M.J.; Zhang, Z.; Danielson, J.J.; Krieger, T.; Curtis, B.; Haase, J.; et al. *ASTER Global Digital Elevation Model Version 2-Summary of Validation Results*, 2nd ed.; NASA: Washington, DC, USA, 2011.
4. Takaku, J.; Tadono, T.; Tsutsui, K. Generation of high resolution global DSM from ALOS PRISM. *Int. Arch. Photogramm. Remote Sens. Spat. Inf. Sci.* **2014**, *XL-4*, 243–248. [[CrossRef](#)]
5. Tadono, T.; Ishida, H.; Oda, F.; Naito, S.; Minakawa, K.; Iwamoto, H. Precise global DEM generation by ALOS PRISM. *ISPRS Ann. Photogramm. Remote Sens. Spat. Inf. Sci.* **2014**, *II-4*, 71–76. [[CrossRef](#)]
6. Krieger, G.; Moreira, A.; Fiedler, H.; Hajnsek, I.; Werner, M.; Younis, M.; Zink, M. Tandem-x: A satellite formation for high-resolution SAR interferometry. *IEEE Geosci. Remote* **2007**, *45*, 3317–3341. [[CrossRef](#)]
7. Rizzoli, P.; Martone, M.; Gonzalez, C.; Wecklich, C.; Tridon, D.B.; Brautigam, B.; Bachmann, M.; Schulze, D.; Fritz, T.; Huber, M.; et al. Generation and performance assessment of the global TanDEM-X digital elevation model. *ISPRS J. Photogramm.* **2017**, *132*, 119–139. [[CrossRef](#)]
8. Sofia, G.; Hillier, J.K.; Conway, S.J. Frontiers in geomorphometry and earth surface dynamics: Possibilities, limitations and perspectives. *Earth Surf. Dyn.* **2016**, *4*, 721–725. [[CrossRef](#)]
9. Dragut, L.; Blaschke, T. Automated classification of landform elements using object-based image analysis. *Geomorphology* **2006**, *81*, 330–344. [[CrossRef](#)]
10. Mokarram, M.; Seif, A.; Sathyamoorthy, D. Landform classification via fuzzy classification of morphometric parameters computed from digital elevation models: Case study on Zagros Mountains. *Arab. J. Geosci.* **2015**, *8*, 4921–4937. [[CrossRef](#)]
11. Kramm, T.; Hoffmeister, D.; Curdt, C.; Maleki, S.; Khormali, F.; Kehl, M. Accuracy assessment of landform classification approaches on different spatial scales for the Iranian Loess Plateau. *ISPRS Int. Geo-Inf.* **2017**, *6*, 366. [[CrossRef](#)]
12. Huang, L.C.; Liu, L.; Jiang, L.M.; Zhang, T.J. Automatic mapping of thermokarst landforms from remote sensing images using deep learning: A case study in the Northeastern Tibetan Plateau. *Remote Sens.* **2018**, *10*, 2067. [[CrossRef](#)]
13. Newman, D.R.; Lindsay, J.B.; Cockburn, J.M.H. Measuring hyperscale topographic anisotropy as a continuous landscape property. *Geosciences* **2018**, *8*, 278.
14. Bishop, M.P.; James, L.A.; Shroder, J.F.; Walsh, S.J. Geospatial technologies and digital geomorphological mapping: Concepts, issues and research. *Geomorphology* **2012**, *137*, 5–26. [[CrossRef](#)]
15. Tarolli, P.; Sofia, G. Human topographic signatures and derived geomorphic processes across landscapes. *Geomorphology* **2016**, *255*, 140–161. [[CrossRef](#)]
16. Schwanghart, W.; Groom, G.; Kuhn, N.J.; Heckrath, G. Flow network derivation from a high resolution DEM in a low relief, agrarian landscape. *Earth Surf. Process. Landf.* **2013**, *38*, 1576–1586. [[CrossRef](#)]
17. Drisya, J.; Kumar, D.S. Comparison of digitally delineated stream networks from different spaceborne digital elevation models: A case study based on two watersheds in South India. *Arab. J. Geosci.* **2016**, *9*, 710. [[CrossRef](#)]
18. Rossman, N.R.; Zlotnik, V.A.; Rowe, C.M. An approach to hydrogeological modeling of a large system of groundwater-fed lakes and wetlands in the Nebraska Sand Hills, USA. *Hydrogeol. J.* **2018**, *26*, 881–897. [[CrossRef](#)]
19. Kalambukattu, J.G.; Kumar, S.; Raj, R.A. Digital soil mapping in a Himalayan watershed using remote sensing and terrain parameters employing artificial neural network model. *Environ. Earth Sci.* **2018**, *77*, 203. [[CrossRef](#)]
20. Marques, K.P.P.; Dematte, J.A.M.; Miller, B.A.; Lepsch, I.F. Geomorphometric segmentation of complex slope elements for detailed digital soil mapping in Southeast Brazil. *Geoderma Reg.* **2018**, *14*, e00175. [[CrossRef](#)]
21. Guo, L.; Shi, T.Z.; Linderman, M.; Chen, Y.Y.; Zhang, H.T.; Fu, P. Exploring the influence of spatial resolution on the digital mapping of soil organic carbon by airborne hyperspectral VNIR imaging. *Remote Sens.* **2019**, *11*, 1032. [[CrossRef](#)]

22. Kellndorfer, J.; Walker, W.; Pierce, L.; Dobson, C.; Fites, J.A.; Hunsaker, C.; Vona, J.; Clutter, M. Vegetation height estimation from shuttle radar topography mission and national elevation datasets. *Remote Sens. Environ.* **2004**, *93*, 339–358. [[CrossRef](#)]
23. Leempoel, K.; Parisod, C.; Geiser, C.; Daprà, L.; Vittoz, P.; Joost, S. Very high-resolution digital elevation models: Are multi-scale derived variables ecologically relevant? *Methods Ecol. Evolut.* **2015**, *6*, 1373–1383. [[CrossRef](#)]
24. Moudry, V.; Lecours, V.; Gdulova, K.; Gabor, L.; Moudra, L.; Kropacek, J.; Wild, J. On the use of global DEMs in ecological modelling and the accuracy of new bare-earth DEMs. *Ecol. Model* **2018**, *383*, 3–9. [[CrossRef](#)]
25. Blaszczyk, M.; Ignatiuk, D.; Grabiec, M.; Kolondra, L.; Laska, M.; Decaux, L.; Jania, J.; Berthier, E.; Luks, B.; Barzycka, B.; et al. Quality assessment and glaciological applications of digital elevation models derived from space-borne and aerial images over two tidewater glaciers of Southern Spitsbergen. *Remote Sens.* **2019**, *11*, 1121. [[CrossRef](#)]
26. Gesch, D.B. Best practices for elevation-based assessments of sea-level rise and coastal flooding exposure. *Front. Earth Sci.* **2018**, *6*, 230. [[CrossRef](#)]
27. Mmbando, G.A.; Kleyer, M. Mapping precipitation, temperature, and evapotranspiration in the Mkomazi River Basin, Tanzania. *Climate* **2018**, *6*, 63. [[CrossRef](#)]
28. Goodchild, M.F. Scale in GIS: An overview. *Geomorphology* **2011**, *130*, 5–9. [[CrossRef](#)]
29. Kienzle, S. The effect of DEM raster resolution on first order, second order and compound terrain derivatives. *Trans. GIS* **2004**, *8*, 83–111. [[CrossRef](#)]
30. Zhang, W.H.; Montgomery, D.R. Digital elevation model grid size, landscape representation, and hydrologic simulations. *Water Resour. Res.* **1994**, *30*, 1019–1028. [[CrossRef](#)]
31. Smith, M.P.; Zhu, A.X.; Burt, J.E.; Stiles, C. The effects of dem resolution and neighborhood size on digital soil survey. *Geoderma* **2006**, *137*, 58–69. [[CrossRef](#)]
32. Sorensen, R.; Seibert, J. Effects of dem resolution on the calculation of topographical indices: TWI and its components. *J. Hydrol.* **2007**, *347*, 79–89. [[CrossRef](#)]
33. Deng, Y.; Wilson, J.P.; Bauer, B.O. DEM resolution dependencies of terrain attributes across a landscape. *Int. J. Geogr. Inf. Sci.* **2007**, *21*, 187–213. [[CrossRef](#)]
34. Kim, D.; Zheng, Y.B. Scale-dependent predictability of DEM-based landform attributes for soil spatial variability in a coastal dune system. *Geoderma* **2011**, *164*, 181–194. [[CrossRef](#)]
35. Grohmann, C.H.; Smith, M.J.; Riccomini, C. Multiscale analysis of topographic surface roughness in the Midland Valley, Scotland. *IEEE Geosci. Remote* **2011**, *49*, 1200–1213. [[CrossRef](#)]
36. Lindsay, J.B.; Cockburn, J.M.H.; Russell, H.A.J. An integral image approach to performing multi-scale topographic position analysis. *Geomorphology* **2015**, *245*, 51–61. [[CrossRef](#)]
37. Newman, D.R.; Lindsay, J.B.; Cockburn, J.M.H. Evaluating metrics of local topographic position for multiscale geomorphometric analysis. *Geomorphology* **2018**, *312*, 40–50. [[CrossRef](#)]
38. Grieve, S.W.D.; Mudd, S.M.; Milodowski, D.T.; Clubb, F.J.; Furbish, D.J. How does grid-resolution modulate the topographic expression of geomorphic processes? *Earth Surf. Dyn.* **2016**, *4*, 627–653. [[CrossRef](#)]
39. Grieve, S.W.D.; Mudd, S.M.; Hurst, M.D.; Milodowski, D.T. A nondimensional framework for exploring the relief structure of landscapes. *Earth Surf. Dyn.* **2016**, *4*, 309–325. [[CrossRef](#)]
40. Zhao, S.M.; Cheng, W.M.; Zhou, C.H.; Chen, X.; Zhang, S.F.; Zhou, Z.P.; Liu, H.J.; Chai, H.X. Accuracy assessment of the ASTER GDEM and SRTM3 DEM: An example in the Loess Plateau and North China Plain of China. *Int. J. Remote Sens.* **2011**, *32*, 8081–8093. [[CrossRef](#)]
41. Suwandana, E.; Kawamura, K.; Sakuno, Y.; Kustiyananto, E.; Raharjo, B. Evaluation of ASTER GDEM2 in comparison with GDEM1, SRTM DEM and topographic-map-derived DEM using inundation area analysis and RTK-DGPS data. *Remote Sens.* **2012**, *4*, 2419–2431. [[CrossRef](#)]
42. Mukherjee, S.; Joshi, P.K.; Mukherjee, S.; Ghosh, A.; Garg, R.D.; Mukhopadhyay, A. Evaluation of vertical accuracy of open source digital elevation model (DEM). *Int. J. Appl. Earth Obs.* **2013**, *21*, 205–217. [[CrossRef](#)]
43. Rexer, M.; Hirt, C. Comparison of free high resolution digital elevation data sets (ASTER GDEM2, SRTM v2.1/v4.1) and validation against accurate heights from the Australian National Gravity database. *Aust. J. Earth Sci.* **2014**, *61*, 213–226. [[CrossRef](#)]
44. Satge, F.; Bonnet, M.P.; Timouk, F.; Calmant, S.; Pillco, R.; Molina, J.; Lavado-Casimiro, W.; Arsen, A.; Cretaux, J.F.; Garnier, J. Accuracy assessment of SRTM v4 and ASTER GDEM v2 over the altiplano watershed using ICESat/GLAS data. *Int. J. Remote Sens.* **2015**, *36*, 465–488. [[CrossRef](#)]

45. Caglar, B.; Becek, K.; Mekik, C.; Ozendi, M. On the vertical accuracy of the ALOS World 3D-30m digital elevation model. *Remote Sens. Lett.* **2018**, *9*, 607–615. [[CrossRef](#)]
46. Wessel, B.; Huber, M.; Wohlfart, C.; Marschalk, U.; Kosmann, D.; Roth, A. Accuracy assessment of the globalTanDEM-X digital elevation model with GPS data. *ISPRS J. Photogramm.* **2018**, *139*, 171–182. [[CrossRef](#)]
47. Altunel, A.O. Evaluation of TanDEM-X 90 m digital elevation model. *Int. J. Remote Sens.* **2019**, *40*, 2841–2854. [[CrossRef](#)]
48. Zhang, K.Q.; Gann, D.; Ross, M.; Biswas, H.; Li, Y.P.; Rhome, J. Comparison of TanDEM-X DEM with LiDAR data for accuracy assessment in a coastal urban area. *Remote Sens.* **2019**, *11*, 876. [[CrossRef](#)]
49. Hu, Z.H.; Peng, J.W.; Hou, Y.L.; Shan, J. Evaluation of recently released open global digital elevation models of Hubei, China. *Remote Sens.* **2017**, *9*, 262. [[CrossRef](#)]
50. Alganci, U.; Besol, B.; Sertel, E. Accuracy assessment of different digital surface models. *ISPRS Int. Geo-Inf.* **2018**, *7*, 114. [[CrossRef](#)]
51. Florinsky, I.; Skrypitsyna, T.; Luschikova, O. Comparative accuracy of the AW3D30 DSM, ASTER GDEM, and SRTM1 DEM: A case study on the Zaoksky testing ground, Central European Russia. *Remote Sens. Lett.* **2018**, *9*, 706–714. [[CrossRef](#)]
52. Jain, A.O.; Thaker, T.; Chaurasia, A.; Patel, P.; Singh, A.K. Vertical accuracy evaluation of SRTM-g11, GDEM-v2, AW3D30 and CartoDEM-v3.1 of 30-m resolution with dual frequency GNSS for Lower Tapi Basin India. *Geocarto Int.* **2018**, *33*, 1237–1256. [[CrossRef](#)]
53. Li, H.; Zhao, J.Y. Evaluation of the newly released worldwide AW3D30 DEM over typical landforms of China using two global DEMs and ICESat/GLAS data. *IEEE J. Sel. Top. Appl. Earth Obs. Remote Sens.* **2018**, *11*, 4430–4440. [[CrossRef](#)]
54. Yahaya, S.I.; El Azzab, D. Vertical accuracy assessment of global digital elevation models and validation of gravity database heights in Niger. *Int. J. Remote Sens.* **2019**, *40*. [[CrossRef](#)]
55. Pipaud, I.; Loibl, D.; Lehmkuhl, F. Evaluation of TanDEM-X elevation data for geomorphological mapping and interpretation in high mountain environments—A case study from SE Tibet, China. *Geomorphology* **2015**, *246*, 232–254. [[CrossRef](#)]
56. Becek, K.; Koppe, W.; Kutoglu, S.H. Evaluation of vertical accuracy of the WorldDEM (tm) using the runway method. *Remote Sens.* **2016**, *8*, 934. [[CrossRef](#)]
57. Podgorski, J.; Kinnard, C.; Petlicki, M.; Urrutia, R. Performance assessment of TanDEM-X DEM for mountain glacier elevation change detection. *Remote Sens.* **2019**, *11*, 187. [[CrossRef](#)]
58. Zhang, K.Q.; Gann, D.; Ross, M.; Robertson, Q.; Sarmiento, J.; Santana, S.; Rhome, J.; Fritz, C. Accuracy assessment of ASTER, SRTM, ALOS, and TDX DEMs for Hispaniola and implications for mapping vulnerability to coastal flooding. *Remote Sens. Environ.* **2019**, *225*, 290–306. [[CrossRef](#)]
59. Purinton, B.; Bookhagen, B. Validation of digital elevation models (DEMs) and comparison of geomorphic metrics on the Southern Central Andean Plateau. *Earth Surf. Dyn.* **2017**, *5*, 211–237. [[CrossRef](#)]
60. Grohmann, C.H. Evaluation of TanDEM-X DEMs on selected Brazilian sites: Comparison with SRTM, ASTER GDEM and ALOS AW3D30. *Remote Sens. Environ.* **2018**, *212*, 121–133. [[CrossRef](#)]
61. Liu, K.; Song, C.Q.; Ke, L.H.; Jiang, L.; Pan, Y.Y.; Ma, R.H. Global open-access DEM performances in earth's most rugged region High Mountain Asia: A multi-level assessment. *Geomorphology* **2019**, *338*, 16–26. [[CrossRef](#)]
62. Holmes, K.W.; Chadwick, O.A.; Kyriakidis, P.C. Error in a USGS 30-meter digital elevation model and its impact on terrain modeling. *J. Hydrol.* **2000**, *233*, 154–173. [[CrossRef](#)]
63. Grohmann, C.H. Effects of spatial resolution on slope and aspect derivation for regional-scale analysis. *Comput. Geosci.* **2015**, *77*, 111–117. [[CrossRef](#)]
64. Houston, J.; Hartley, A.J. The Central Andean west-slope rainshadow and its potential contribution to the origin of hyper-aridity in the Atacama Desert. *Int. J. Climatol.* **2003**, *23*, 1453–1464. [[CrossRef](#)]
65. Hartley, A.J.; Chong, G.; Houston, J.; Mather, A.E. 150 million years of climatic stability: Evidence from the Atacama Desert, Northern Chile. *J. Geol. Soc.* **2005**, *162*, 421–424. [[CrossRef](#)]
66. Dunai, T.J.; Lopez, G.A.G.; Juez-Larre, J. Oligocene-Miocene age of aridity in the Atacama Desert revealed by exposure dating of erosion-sensitive landforms. *Geology* **2005**, *33*, 321–324. [[CrossRef](#)]
67. Walk, J.; Stauch, G.; Reyers, M.; Vásquez, P.; Sepúlveda, F.A.; Bartz, M.; Hoffmeister, D.; Brückner, H.; Lehmkuhl, F. Gradients in climate, geology, and topography affecting coastal alluvial fan morphodynamics in hyperarid regions—the Atacama perspective. *Glob. Planet Chang.* **2019**. [[CrossRef](#)]

68. May, S.M.; Hoffmeister, D.; Wolf, D.; Bubenzer, O. Zebra stripes in the Atacama Desert revisited—granular fingering as a mechanism for zebra stripe formation? *Geomorphology* **2019**, *344*, 46–59. [[CrossRef](#)]
69. Abrams, M.; Bailey, B.; Tsu, H.; Hato, M. The ASTER Global DEM. *Photogramm. Eng. Remote Sens.* **2010**, *76*, 344–348.
70. Hirano, A.; Welch, R.; Lang, H. Mapping from ASTER stereo image data: DEM validation and accuracy assessment. *ISPRS J. Photogramm. Remote Sens.* **2003**, *57*, 356–370. [[CrossRef](#)]
71. Abrams, M.; Crippen, R. *ASTER GDEM v3 (ASTER Global DEM); User Guide*; California Institute of Technology: Pasadena, CA, USA, 2019.
72. Tadono, T.; Shimada, M.; Murakami, H.; Takaku, J. Calibration of PRISM and AVNIR-2 onboard ALOS “daichi”. *IEEE Geosci. Remote* **2009**, *47*, 4042–4050. [[CrossRef](#)]
73. Takaku, J.; Tadono, T. Quality updates of ‘AW3D’ Global DSM generated from ALOS PRISM. In Proceedings of the 2017 IEEE International Geoscience and Remote Sensing Symposium (IGARSS), Fort Worth, TX, USA, 23–28 July 2017; pp. 5666–5669.
74. Rodríguez, E.; Morris, C.S.; Belz, J.E.; Chapin, E.C.; Martin, J.M.; Daffer, W.; Hensley, S. *An Assessment of the SRTM Topographic Products*; Jet Propulsion Laboratory (JPL): Pasadena, CA, USA, 2005.
75. Reuter, H.I.; Nelson, A.; Jarvis, A. An evaluation of void-filling interpolation methods for SRTM data. *Int. J. Geogr. Inf. Sci.* **2007**, *21*, 983–1008. [[CrossRef](#)]
76. Wessel, B. *TanDEM-X Ground Segment—DEM Products Specification Document*; EOC: Munich, Germany, 2016.
77. Rizzoli, P.; Brautigam, B.; Kraus, T.; Martone, M.; Krieger, G. Relative height error analysis of TanDEM-X elevation data. *ISPRS J. Photogramm.* **2012**, *73*, 30–38. [[CrossRef](#)]
78. Keys, L.; Baade, J. Uncertainty in catchment delineations as a result of digital elevation model choice. *Hydrology* **2019**, *6*, 13. [[CrossRef](#)]
79. Astrium GEO-Information Services. *Pléiades Imagery User Guide V 2.0*; Astrium: Paris, France, 2012.
80. De Lussy, F.; Kubik, P.; Greslou, D.; Pascal, V.; Gigord, P.; Cantou, J.P. Pleiades-HR image system products and quality. Pleiades-HR image system products and geometric accuracy. In Proceedings of the ISPRS Hannover Workshop, Hannover, Germany, 17–20 May 2005.
81. Gleyzes, M.A.; Perret, L.; Kubik, P. Pleiades system architecture and main performances. *Int. Arch. Photogramm. Remote Sens. Spat. Inf. Sci.* **2012**, *39*, 537–542. [[CrossRef](#)]
82. Poli, D.; Remondino, F.; Angiuli, E.; Agugiaro, G. Evaluation of Pleiades-1a triplet on Trento testfield. *Int. Arch. Photogramm. Remote Sens. Spat. Inf. Sci.* **2013**, *XL-1/W1*, 287–292. [[CrossRef](#)]
83. Rieg, L.; Klug, C.; Nicholson, L.; Sailer, R. Pleiades tri-stereo data for glacier investigations—examples from the European Alps and the Khumbu Himal. *Remote Sens.* **2018**, *10*, 1563. [[CrossRef](#)]
84. Astrium GEO-Information Services. *SPOT 6 & SPOT 7 Imagery—User Guide*; Astrium: Paris, France, 2013.
85. Maune, D.F. *Digital Elevation Model Technologies and Applications: The DEM Users Manual*, 2nd ed.; American Society for Photogrammetry and Remote Sensing: Bethesda, MD, USA, 2007; 655p.
86. Schutz, B.E.; Zwally, H.J.; Shuman, C.A.; Hancock, D.; DiMarzio, J.P. Overview of the ICESat mission. *Geophys. Res. Lett.* **2005**, *32*, L21S01. [[CrossRef](#)]
87. Zwally, H.J.; Schutz, B.; Abdalati, W.; Abshire, J.; Bentley, C.; Brenner, A.; Bufton, J.; Dezio, J.; Hancock, D.; Harding, D.; et al. ICESat’s laser measurements of polar ice, atmosphere, ocean, and land. *J. Geodyn.* **2002**, *34*, 405–445. [[CrossRef](#)]
88. Duong, H.; Lindenbergh, R.; Pfeifer, N.; Vosselman, G. ICESat full-waveform altimetry compared to airborne laser scanning altimetry over The Netherlands. *IEEE Trans. Geosci. Remote* **2009**, *47*, 3365–3378. [[CrossRef](#)]
89. Huang, X.D.; Xie, H.J.; Liang, T.G.; Yi, D.H. Estimating vertical error of SRTM and map-based DEMs using ICESat altimetry data in the Eastern Tibetan Plateau. *Int. J. Remote Sens.* **2011**, *32*, 5177–5196. [[CrossRef](#)]
90. Zhao, S.M.; Cheng, W.M.; Zhou, C.H.; Liu, H.J.; Su, Q.M.; Zhang, S.F.; He, W.C.; Wang, L.; Wu, W.J. Using MLR to model the vertical error distribution of ASTER GDEM v2 data based on ICESat/GLA14 data in the Loess Plateau of China. *Z. Geomorphol.* **2017**, *61*, 9–26. [[CrossRef](#)]
91. Baghdadi, N.; Lemarquand, N.; Abdallah, H.; Bailly, J.S. The relevance of GLAS/ICESat elevation data for the monitoring of river networks. *Remote Sens.* **2011**, *3*, 708–720. [[CrossRef](#)]
92. Markus, T.; Neumann, T.; Martino, A.; Abdalati, W.; Brunt, K.; Csatho, B.; Farrell, S.; Fricker, H.; Gardner, A.; Harding, D.; et al. The ice, cloud, and land elevation satellite-2 (ICESat-2): Science requirements, concept, and implementation. *Remote Sens. Environ.* **2017**, *190*, 260–273. [[CrossRef](#)]

93. Neuenschwander, A.; Pitts, K. The ALT08 land and vegetation product for the ICESat-2 mission. *Remote Sens. Environ.* **2019**, *221*, 247–259. [[CrossRef](#)]
94. Neuenschwander, L.A.; Magruder, A.L. Canopy and terrain height retrievals with ICESat-2: A first look. *Remote Sens.* **2019**, *11*, 1721. [[CrossRef](#)]
95. Lague, D.; Brodu, N.; Leroux, J. Accurate 3D comparison of complex topography with terrestrial laser scanner: Application to the Rangitikei Canyon (N-Z). *ISPRS J. Photogramm.* **2013**, *82*, 10–26. [[CrossRef](#)]
96. Höhle, J.; Höhle, M. Accuracy assessment of digital elevation models by means of robust statistical methods. *ISPRS J. Photogramm.* **2009**, *64*, 398–406. [[CrossRef](#)]
97. Riley, S.J.; DeGloria, S.D.; Elliot, R. A terrain ruggedness index that quantifies topographic heterogeneity. *Int. J. Sci.* **1999**, *5*, 23–27.
98. Weiss, A.D. Topographic position and landforms analysis. In *ESRI Users Conference*; ESRI: San Diego, CA, USA, 2001.
99. Boulton, S.J.; Stokes, M. Which DEM is best for analyzing fluvial landscape development in mountainous terrains? *Geomorphology* **2018**, *310*, 168–187. [[CrossRef](#)]
100. Huber, M.; Wessel, B.; Kosmann, D.; Felbier, A.; Schwieger, V.; Habermeyer, M.; Wendleder, A.; Roth, A. Ensuring globally the TanDEM-X height accuracy: Analysis of the reference data sets ICESat, SRTM and KGPS-tracks. In *Proceedings of the 2009 IEEE International Geoscience and Remote Sensing Symposium (IGARSS)*, Cape Town, South Africa, 12–17 July 2009; pp. II-769–II-772.
101. Gruber, A.; Wessel, B.; Huber, M.; Roth, A. Operational TanDEM-X DEM calibration and first validation results. *ISPRS J. Photogramm.* **2012**, *73*, 39–49. [[CrossRef](#)]
102. Takaku, J.; Tadono, T.; Tsutsui, K.; Ichikawa, M. Validation of 'AW3D' Global DSM generated from ALOS PRISM. In *Proceedings of the XXIII ISPRS Congress*, Prague, Czech Republic, 12–19 July 2016.
103. Graf, L.; Moreno-de-las-Heras, M.; Ruiz, M.; Calsamiglia, A.; Garcia-Comendador, J.; Fortesa, J.; Lopez-Tarazon, J.A.; Estrany, J. Accuracy assessment of digital terrain model dataset sources for hydrogeomorphological modelling in small Mediterranean catchments. *Remote Sens.* **2018**, *10*, 2014. [[CrossRef](#)]
104. Mouratidis, A.; Ampatzidis, D. European digital elevation model validation against extensive global navigation satellite systems data and comparison with SRTM DEM and ASTER GDEM in Central Macedonia (Greece). *ISPRS Int. Geo-Inf.* **2019**, *8*, 108. [[CrossRef](#)]



© 2019 by the authors. Licensee MDPI, Basel, Switzerland. This article is an open access article distributed under the terms and conditions of the Creative Commons Attribution (CC BY) license (<http://creativecommons.org/licenses/by/4.0/>).